ORIGINAL PAPER

Synthesis, characterization, electrochemical studies and antimicrobial activities of metal complexes

A. Z. El-Sonbati[1] · M. A. Diab[1] · M. I. Abou-Dobara[2] · A. M. Eldesoky[3,4] · H. R. Issa[1]

Abstract

Metal complexes of Schiff base 4-[(2, 4-dihydroxy-benzylidene)-amino]-1, 5-dimethyl-2-phenyl-1, 2-dihydroxo-pyrazol-3-one (H_2L) derived from condensation of 2,4-dihydroxybenzaldehyde and 4-aminoantipyrine were synthesized and characterized by FT-IR spectra, elemental analysis, ^1H & ^{13}C NMR, mass spectra, UV–Visible, X-ray diffraction, molar conductance, magnetic moment and thermal analysis (TGA). The elemental analysis proved that the complexes have the general formulae of $[M(HL)(X)(OH_2)]_2$, where $M = Cu(II)$; $X = OAc^-$ (**1**); NO_3^- (**2**); Cl^- (**3**), $M = Co(II)$ (**4**), $Mn(II)$ (**5**); $X = OAc$ and $\{[UO_2(HL)]_2.2(OAc)\}$(**6**). According to the FT-IR spectra data, it was found that the H_2L ligand is coordinated to the metal ions in a tridentate donor sites of the nitrogen atom of azomethine group, the oxygen atom of phenolic group and the oxygen atom of carbonyl group. From the measurements of magnetic susceptibility and electronic spectral data, it is found that these complexes are octahedral geometries. The trend in g value ($g_\parallel > g_\perp > 2.00$) suggests that the unpaired electron on copper has d_{x2-y2} character and the complexes have an octahedral structure. By comparing the synthesized ligand (H_2L) to its metal complexes was screened for their antibacterial activity against *Klebsiella pneumoniae, Escherichia coli*, *Pseudomonas* sp., *Bacillus cereus* and *Staphylococcus aureus*. It was found that the metal complexes had more potent antimicrobial than the parent Schiff base ligand against one or more microbial species. Some complexes showed higher activity than ligand. The complex (**3**) has antibacterial activities against *Bacillus cereus, Klebsiella pneumoniae* and *Staphylococcus aureus*. The antibacterial activity of complex (**3**) was the highest ones than the ligand and other complexes as well as penicillin G against *Klebsiella pneumoniae*. Antifungal activities were determined against *Fusarium oxysporum, Aspergillus niger* and *Candida albicans*. The inhibition efficiency of the prepared ligand (**H_2L**) against the corrosion of carbon steel in HCl (2 M) solution was determined by various electrochemical techniques.

Keywords Schiff base-metal chelates · Thermal analysis · Antimicrobial activity · Molecular docking · Corrosion inhibition of C-steel

Introduction

Schiff bases are considered as a very important class of organic compounds which have wide applications in many biological aspects [1–3]. The Schiff base complexes have wide applications in analytical and biological chemistry [4, 5]. The tridentate Schiff base formed stable complexes through ONO donor set [1–6].

The presence of *o*-hydroxy group has been regarded as one of the important elements which favor intra-molecular hydrogen bonding (O–HN and OH–N) and also the formation of either enol–imino or keto–amino tautomers [7–9]. Tautomerism in 2-hydroxy-1-naphthaldehyde [10–13]. The transition metal coordinated with nitrogen donor Schiff base to form complexes has received great applications in bioinorganic chemistry [14–16] and is

✉ A. Z. El-Sonbati
  elsonbatisch@yahoo.com

1 Chemistry Department, Faculty of Science, Damietta University, Damietta, Egypt

2 Botany and Microbiology Department, Faculty of Science, Damietta University, Damietta, Egypt

3 Engineering Chemistry Department, High Institute of Engineering & Technology, New Damietta, Egypt

4 Al-Qunfudah Center for Scientific Research (QCSR), Chemistry Department, Al-Qunfudah University College, Umm Al-Qura University, Mecca, Saudi Arabia

applied in various activities such as antimicrobial and antifungal as well as anticancer and antibiotic agents [16–18].

Schiff bases are known to exhibit a broad range of biological activities including antifungal, antibacterial, larvicidal, antimalaria, antiproliferative, antiinflammatory, antiviral and antipyretic properties [19]. The biological and physical properties exhibited by Schiff bases are directly related to the presence of intramolecular H-bonding and as well as proton transfer equilibrium [20]. It is well known that the Schiff bases formed when any primary amine reacts with aldehydes or ketones. The azomethine or imine groups are present in various natural, natural derived or artificial compounds [21, 22].

Recently transition metal complexes with salen ligand derived from the condensation of 2, 4-dihydroxy benzaldehyde with amine have been widely studied. The metal complexes have been attractive area of research, in view of their significance as biomimetic catalysts in the process of oxygenation [23]. Schiff bases have been widely used as ligands because of high stability of the coordination compounds. The π-system in Schiff bases often imposes a geometrical constriction and affects the electronic structure as well. They reported on a wide range of activities such as identify tumors, bacteria and fungi activities. Particular properties of these compounds are due to their chelating ability and bonding modes to the central metal atom. The imine group (-N=CH-) becomes a suitable donor for coordination to grant. The versatile ligands show chelating behavior and various biological properties. 4-amino-antiopyrine has exposed class of compounds that have multi-donor ligands still growing attracts in the research group. A strong interact with the heterocyclic aldehydes or ketenes depending upon coordination with ligand and complexes has stable bioactivities.

The synthesis, characterization and biological activities of some metal(II) complexes of Schiff bases have been reported [17]. This article deals with the synthesis of a novel Schiff base ligand containing carbonyl and azomethine groups as potential chelating sites, namely 4-[(2,4-dihydroxy-benzylidene)-amino]-1,5-dimethyl-2-phenyl-1,2-dihydroxo-pyrazol-3-one (H_2L). In order to explore the ligational behavior of this ligand, a series of H_2L and its Cu(II), Co(II), Mn(II) and UO_2(II) complexes have been prepared and characterized by various physicochemical techniques and their antimicrobial activities were studied. Study of the docking of the H_2L Schiff base ligand, as well as molecular and electronic structures of H_2L and its Cu(II), Co(II), Mn(II) and UO_2(II) complexes are discussed. A study of the inhibition process of H_2L Schiff base ligand against the corrosion of carbon steel

in HCl (2 M) solution was determined by various electrochemical techniques.

Experimental

Materials and methods

All the chemicals and solvents used were purified and dried by standard methods [17, 18, 24, 25]. All measurements were carried out as reported earlier [25–28].

Preparation of H_2L and its complexes

4-[(2,4-Dihydroxy-benzylidene)-amino]-1,5-dimethyl-2-phenyl-1,2-dihydroxo-pyrazol-3-one (H_2L) and its complexes were prepared according to the previously reported method [1, 3, 8, 16]. The purity of ligand was checked by TLC. Our synthetic route of Schiff base ligand is shown in Fig. S1. Elemental Anal. Calc. for $C_{18}H_{17}N_3O_3$: C, 66.87; H, 5.26; N, 13.00%. Found C, 66. 68; H, 5. 19; N, 12.78%. IR: υ (CH=N), 1581; υ (C =O), 1614 and υ (C-O), 1362 cm^{-1}. ^{1}H NMR: 9.55 (H-7, s); 6.50 (H-3), d); 6.58 (H-5, d); 6.50 (H-6, d); 2.48 (H-10, s); 3.39 (H-11, s); 13.24 (H-4, s); 13.35(H-2,s); 7.24 (H-14,s),; 7.30 (H-18,s); 7.39 (H-15, s); 7.55 (H-17, s) and 7.78 ppm (H-16, s).

Molecular docking analysis

The molecular docking of the H_2L ligand was performed for different bacterial cell division proteins and calculated using Docking Server [29–32]. The calculations of molecular docking were carried out on the receptor of the crystal structure of 3q8u as *Staphylococcus aureus* and the receptor of the crystal structure of 3t88 as *Escherichia coli* proteins model.

Assay of antimicrobial activities

Agar well diffusion method [14, 33, 34] was used to assay the antimicrobial activity of H_2L and its metal complexes at different concentrations (50, 100 and 150 µg/mL) using dimethylformamide (DMF) as solvent. DMF was also tested as a control. The antibacterial activities against *Staphylococcus aureus, Bacillus cereus*, *Klebsiella pneumoniae, Escherichia coli* and *Pseudomonas* sp. were assayed on nutrient agar medium. The antifungal activities were assayed against *Aspergillus niger*, *Candida albicans* and *Fusarium oxysporum* using DOX agar medium. Wells (10 mm) were inoculated with the tested bacteria or fungi in agar medium. Each tested compound (200 µL) was put in a well. The agar plates were kept at 4 °C for 30 min.,

then incubated them at 37 and 30 °C for bacteria and fungi, respectively, the diameters of the inhibition zones of activities of antimicrobial are measured after 24 h and 7 days for bacteria and fungi, respectively. The standard drugs (penicillin and miconazole) were also tested in comparison with the compounds.

Corrosion measurements

Metal coupons composition and medium

Corrosion measurements were used the C-steel. Its composition (wt%) is 0.20 C, 0.30 Si, 0.53 Mn, 0.055S, 0.045P, Fe balance. The test solution of 2 M HCl was prepared by dilution of HCl (BDH grade, 37%) with double distilled water.

Electrochemical measurements

Gamry instrument PCI300/4 Potentiostat/Galvanostat/Zra analyzer, EIS300 electrochemical impedance, DC105 corrosion software, spectroscopy software, EFM140 electrochemical frequency modulation software and Echem Analyst 5.5 for plotting results, graphing, data fitting and calculating were used for all electrochemical experiments.

Electrochemical Frequency Modulation technique (EFM) EFM measurements were carried out using potential perturbation signal (10 mV amplitude and 2 and 5 Hz sine waves). These two frequencies were chosen because of three arguments. i_{corr}, corrosion current density, β_c and β_a, Tafel slopes, and CF-3, the causality factors, were calculated using the larger peaks [35].

Electrochemical Impedance Spectroscopy (EIS) EIS measurements were performed using AC signals of 5 mV

peak-to-peak amplitude at the open-circuit potential in the frequency range of 100 kHz to 0.1 Hz.

Potentiodynamic polarization measurements Potentiodynamic polarization measurements were recorded in using a typical three-compartment glass cell consisted of:

1. Carbon steel specimen (1 cm^2) welded from one side to copper wire for electric connection as working electrode.
2. Saturated calomel electrode (SCE) as a reference electrode.
3. A platinum foil (1 cm^2) as a counter electrode.

By applying different electrode potential ranging from −800 to 500 mV *vs.* SCE, Tafel polarization curves were obtained. The determination of corrosion current is performed by extrapolation of the anodic and cathodic of Tafel lines by using Stern-Geary method [36, 37].

Results and discussion

The Schiff base, H$_2$L (Scheme 1), was synthesized by the direct condensation of 2,4-dihydroxy benzaldehyde with 4-aminoantipyrine. The elemental analyses data obtained were in good agreement with the stoichiometry of 4-[(2, 4-dihydroxy-benzylidene)-amino]-1,5-dimethyl-2-phenyl-1,2-dihydroxo-pyrazol-3-one (H$_2$L) (see section Experimental). The ligand can exist in two tautomeric forms, keto and keto-hydrazo forms due to the presence of OH, HC=N and C=O functional groups (Fig. S1). However, the spectral studies reveal the existence of keto in the solid state. The Cu(II), Co(II), Mn(II) and UO$_2$(II) complexes were obtained by a general method using ethanolic solution of metal ions and solution of ligand

4-Aminoantipyrine   2,4-Dihydroxybenzaldehyde   Schiff base ligand (H$_2$L)
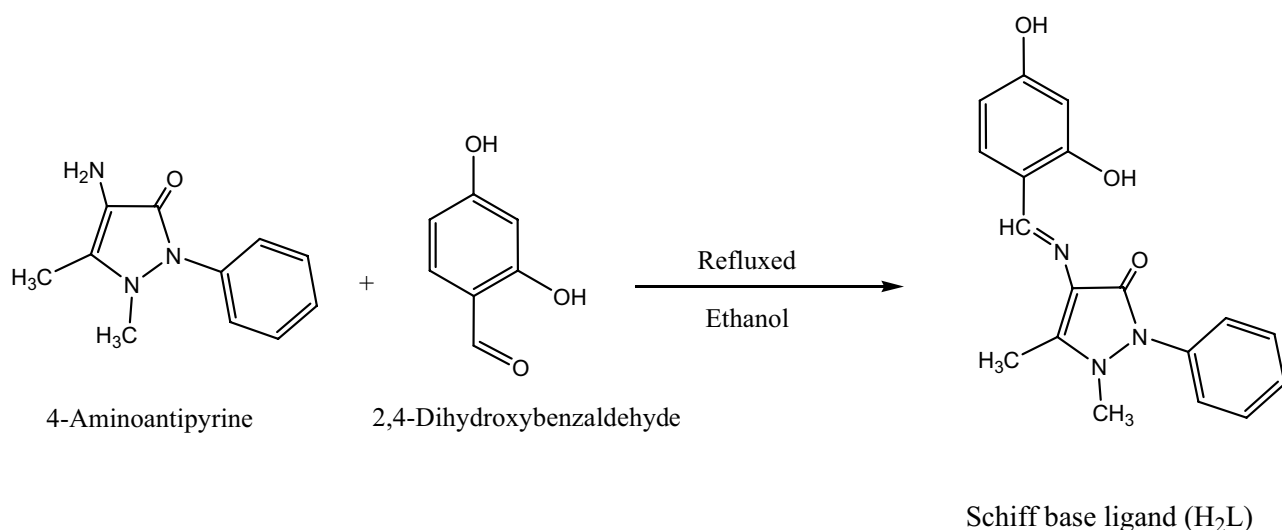
Scheme 1 The formation reaction of the Schiff base ligand (H$_2$L)

in absolute ethanol in 1:1 molar ratio. Five chelate rings were formed by metal(II) coordination to tridentate Schiff base (ONO). The ring formations determine a higher stability of the compounds [38]. The ligand and its complexes were formed only in the powder form, which was not suitable for single X-ray diffraction analysis. Further attempts to get crystals were not successful. Single crystals of the compounds could not be isolated from any organic solution; thus, no definite structures are described. However, the analytical and spectroscopic data enable as to predict possible structures as shown below.

The ligand (H_2L) on interaction with metal(II) salts yielded complexes corresponding to the general formulae $[M(HL)(X)(OH_2)]_2$ and $\{[UO_2(HL)]_2 . 2(OAc)\}$ as obtainable in the following reaction.

$H_2L + MX_2.nH_2O \rightarrow [M(HL)(X)(OH_2)]_2$, where $M = Cu(II)$; $X = OAc^-$ (**1**); NO_3^- (**2**); Cl^- (**3**), $M = Co(II)$ (**4**), Mn(II) (**5**); $X = OAc$.

$H_2L + MX_2.nH_2O \rightarrow \{[UO_2(HL)]_2 . 2(OAc)\}$ (6).

All the complexes are colored, high melting point. They are insoluble in common organic solvents and only soluble in DMF and DMSO. The molar conductance values of the soluble complexes in DMSO (10^{-3} M solution at 25 °C) indicate that all the complexes (**1–5**) were found to be non-electrolytes [39] (Table 1) which indicate that the anion and the ligands were coordinated to the central M(II). But the molar conductance value of compound (**6**) is $31\,\Omega^{-1}\,mol^{-1}\,cm^{-1}$ which is consistent with the value of 1:1 electrolyte as suggested by the formula.

Spectroscopic study

^{1}H and ^{13}C NMR spectra

The ^{1}H-NMR and ^{13}C-NMR chemical shifts (ppm) gave a good support to the suggested structure. The ^{1}H-NMR spectrum of ligand (H_2L) was recorded in DMSO-d_6 at room temperature as shown in Table 2, showing doublets/multiplets peaks in the range ~ 6.50–7.78 ppm (Fig. S2) due to aryl protons of benzene rings. Another singlet peak corresponding to two proton of OH groups are observed in the range ~ 13.24–13.35 ppm. This signal was disappeared when a D_2O exchange experiment was carried out (Fig. S3). The resonance of imine proton downfield shifted to (~ 9.55 ppm) due to the strong shielding effect of the hydroxyl groups, $= C–CH_3$ at 2.48 and $-N-CH_3$ at 3.39 ppm. The ^{13}C-NMR spectrum showed the appearance of peaks at 120, 160, 118, 115, 135, 134, 160, 116, 133, 10, 35, 160, 142, 112, 129, 119, 130 and 113 ppm. for C1-C18, respectively.
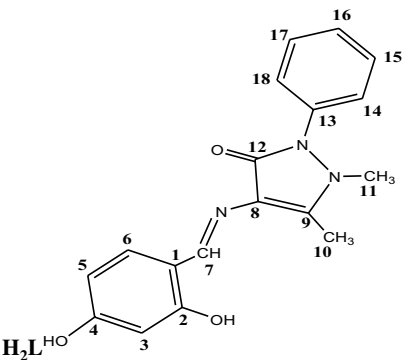
Infrared spectral studies

The important FT-IR peaks of H_2L and its metal complexes are described in Table 3 and Figs. S4-S7. The infrared spectrum of H_2L shows the appearance of a single band assigned to $C = N$ stretching mode of Schiff base at 1581 cm^{-1} [40]. This band was shifted to lower or higher wave numbers ranging from 1583 to 1574 cm^{-1} in the spectra of all complexes, indicating the participation of the nitrogen atom of the azomethine group in coordination. The infrared spectra of all the complexes show a considerable shift in the carbonyl (pyrazolone) absorption $\Delta v(C = O)$ by 6–30 cm^{-1}, indicating a decrease in the stretching force constant of ($C = O$) as a consequence of coordination through the oxygen atom of the free Schiff base. The $C = O$ stretching occurs at 1614 cm^{-1} in the Schiff base [3] and has been observed at 1608–1580 cm^{-1} in all of the complexes. This exceptionally high shifted to lower frequency of the carbonyl frequency may be

Table 1 Elemental analysis data, magnetic susceptibility and molar conductivity of complexes

Compound	Found/Cal.)%				μ_{eff}^* (B.M.)	Molar conductance (Ω^{-1} cm^2 mol^{-1})
	C	H	N	M		
$[Cu(HL)(H_2O)(OAc)]_2$ (1)	51.66 (51.87)	4.39 (4.51)	8.78 (9.08)	13.60 (13.74)	1.92	2.80
$[Cu(HL)(H_2O)(ONO_2)]_2$ (2)	46.28 (46.40)	3.65 (3.87)	11.77 (12.03)	13.47 (13.65)	1.85	3.50
$[Cu(HL)(H_2O)(Cl)]_2$ (3)	49.10 (49.20)	3.88 (4.10)	9.39 (9.57)	14.28 (14.47)	1.90	4.50
$[Co(HL)(H_2O)(OAc)]_2$ (4)	52.34 (52.41)	4.45 (4.59)	8.87 (9.17)	12.59 (12.87)	4.67	5.50
$[Mn(HL)(H_2O)(OAc)]_2$ (5)	52 (52.87)	4.51 (4.63)	9.05 (9.25)	11.86 (12.12)	5.89	7.50
$\{[UO_2(HL)]_2 . 2(OAc)\}$ (6)	36.68 (36.87)	2.66 (2.77)	6.33 (6.45)	36.23 (36.56)	Dia	31.00

*The order of μ_{eff} is $[Cu(HL)(H_2O)(OAc)]_2 > [Cu(HL)(H_2O)(Cl)]_2 > [Cu(HL)(H_2O)(ONO_2)]_2$. $^+$per metal, measured at room temperature

Table 2 ^{1}H and ^{13}C NMR spectrum data of the ligand (H$_2$L) (in ppm)

Compound	^{1}H NMR
	2.48 (s, 3H, H-10), 3,39 (s, 3H, H-11), ~6.50 (d, 1H, H-3), 6.58 (d, 1H, H-5), 6.50 (s, 1H, H-6), 13.24 (s, 1H, H-4), 9.55 (s, 1H, H-7), ~13.24 (s, 1H, H-2)
	^{13}C NMR
	120 (C-1), 160 (C-2), 118 (C-3), 115 (C-4), 135 (C-5), 134 (C-6), 160 (C-7), 116 (C-8), 134 (C-9), 10 (C-10), 35 (C-11), 160 (C-12), 142 (C-13), 112 (C-14), 129 (C-15), 119(-16), 129 (C-17), 112 (C-18)

attributed to the greater flow of electron from the carbonyl group to the bivalent metal due to greater delocalization of the positive charge on the nitrogen atom [41–44]. The free ν(2-OH) is generally observed at ~ 3482 cm^{-1}. The formation of intrahydrogen bonding in fact supports planar pattern of the ligand [45, 46]. In the spectra of the complexes, the absence of a last band indicates the cleavage of the hydrogen bond through the deprotonated phenolic (C$_2$-O-), the deprotonation occurs prior to coordination. The strong band at 1362 cm^{-1} assigned to ν(C-O) in the free Schiff base will shift to higher frequency upon coordination with metal ions. This shift was attributed to the participation of oxygen in coordination [47]. As the shift in case of ν(C-O) is high (~ 50 cm^{-1}), it is assumed that the oxygen of this group acts as a bridge center [48]. In the IR spectra of all complexes, a range of new bands at 720–744, 825–835 and 3389–3485 cm^{-1} due to the wagging, rocking and stretching mode of δ(O–H) vibration, respectively, of coordinated water molecule in the metal complexes [45, 49–51]. There are FT-IR bands in the region 1440–1496 and 1319–1224 cm^{-1} due to asymmetric (ν_{as}) and symmetric (ν_s) stretching vibrations of acetate groups, respectively, for the metal acetate complexes. The $\Delta\nu$ value, i.e., 185–271 cm^{-1} suggests the unidentate coordination of acetation. The weak bands far FT-IR spectrum in the region 550–590 and 445–470 cm^{-1} attributed to ν (M–O) and ν (M–N) vibrations, respectively. The infrared spectrum of complex (2) exhibits bands in the range 1543, 1289 and 1125 cm^{-1} attributed to ν(N = O), ν_{asym}(NO$_2$) and ν_{sym}(NO$_2$), respectively, which are corresponding to nature of coordinated monodentate nitrate group [3].

Mass spectra

The mass spectra of the H$_2$L ligand and Cu(II), Co(II) and Mn(II) complexes **(1,4 and 5)** are shown in Schemes S1–S4 and the ligand exhibits a parents molecular ion peak at m/z = 323 amu and is equal to the formula weight of

Table 3 Position of FT-IR spectral bands (cm^{-1}) in Schiff base ligand (H$_2$L) and its metal complexes

Compd.^{a}	C=O	C=N	OH	C-O	M–O	M–N	Anions
H$_2$L	1614	1581	3482	1362	–	–	–
(1)	1608	1583	–	1402	555	470	1440, 1236
(2)	1594	1580	–	1403	560	465	1543,1289 1125
(3)	1591	1577	–	145	570	450	
(4)	1594	1574	–	1424	580	465	1496, 1319
(5)	1585	1566	–	1416	585	460	1495, 1224
(6)	1618	1570	–	1410	575	455	

^{a}Numbers as given in Table 1

the H_2L ligand $[C_{18}H_{17}N_3O_3]$. The peak at m/z = 295 amu formed from the H_2L ligand through the removal of atoms $[C_2H_4O]$ (Scheme S1 and Fig. S8). The undergoes fragment by the removal of atoms $[C_{10}H_9N_3O_3]$ and giving molecular ion peak at m/z = 76 amu that represent C_6H_4 fragment.

For Cu(II) complex (1), the ion of m/z = 462.54 amu undergoes fragmentation to a stable peak at m/z = 324.54, 233.54, 218 and 76 amu by losing $2H_2O + C_4H_8NO_2$, C_6H_5N, $C_3 + CuO$ and CNO atoms, respectively, (Scheme S2 and Fig. S9).

For Cu(II) complex (4), the ion of m/z = 457.93 amu undergoes fragmentation to a stable peak at m/z = 320.93, 244.93, 217.93, 119 and 77 amu by losing $2H_2O + C_4H_7NO_2$, C_6H_4, CHN, $C_2 + CoO$ and CNO atoms, respectively (Scheme S3 and Fig. S10).

For Mn(II) complex (5), the ion of m/z = 453.94 amu undergoes fragmentation to a peak at m/z = 354.94, 303.94, 214.94, 120 and 78 amu by losing $2H_2O + C_2H_7O_2$, C_3HN, C_6H_3N, $C_2 + MnO$ and CNO atoms, respectively (Scheme S4 and Fig. S11).

Magnetic susceptibility

The measurements of magnetic susceptibility supply information to support the electronic structure of the prepared complexes. The measurement of magnetic susceptibility was calculated by the following relation [52]:

$\mu_{eff.} = 2.83\sqrt{X`_M T}$ where T is the temperature (K), μ_{eff}, the magnetic moment in Bohr Magneton (BM).

$X`_M = X_M - $ (diamag. corr).

X_M molar magnetic susceptibility, $X`_M$ after correction. Magnetic susceptibility measurements represented that the complexes (1–5) have paramagnetic character and suggested the octahedral structures of the complexes [26, 53].

Electronic spectra

The UV/Vis absorption spectrum of the ligand (H_2L) displays mainly four bands. The first band located at ~ 34,480 cm^{-1} can be assigned to the moderate energy (π-π*) transition of the aromatic ring (^1L_a-^1A) [54], while the second band at ~ 30,250 cm^{-1} is due to low energy (π-π*) transition corresponding to the (^1L_b-^1A) state [54]. The third

band located at ~ 26,500 cm^{-1} corresponds to (π-π*) transition involving the π-electron of the azomethine group [55]. The very broad band appear in the range ~ 20,080 cm^{-1} can be assigned to an intramolecular charge transfer interaction (CT) involving the whole molecule [54] as given in Fig. S1. Thus, the band of intramolecular charge transfer interaction can be considered as a composite band resulting from the absorption of the two equilibrium species. The absorption region on the lower energy site would be due to the keto-hydroxy form while that at higher energy region can be attributed to the absorption by the keto-hydrazone species [55, 56].

The electronic absorption spectral data (cm^{-1}) of the complexes are listed in Table 4.

The electronic spectrum of Co(II) complex shows three d-d bands at 9540 ($^4T_{1g}$ (F) → $^4T_{2g}$(F)), 16,418 ($^4T_{1g}$ → $^4A_{2g}$) and 19,045 cm^{-1} ($^4T_{1g}$(F) → $^4T_{1g}$(P)) transitions [16], and the magnetic moments (4.67 B.M.) supporting octahedral geometry [57]. The electronic spectrum of Mn(II) complex shows bands 18,620 ($^6A_{1g}$ → $^4T_{1g}$), 21,385 ($^6A_{1g}$ → $^4A_{1g}$), 25,975 ($^6A_{1g}$ → ^4E_g) and 35,845 cm^{-1} ($^6A_{1g}$ → $^4T_{1g}$), suggesting octahedral symmetry in the complex [16]. Various ligand field parameters 10Dq, B, C, β, F_2, F_4 have also been calculated using Konig's method [58].

The calculated values of ligand field splitting energy, 10Dq, the nephelauxetic ratio (β), the Racah inter-electronic repulsion parameter, B, and the ratio υ_2/υ_1 (Table 4) supports the proposed geometry for all the synthesized Co(II) and Mn(II) octahedral complexes. The nephelauxetic ratio (β) for Co(II) and Mn(II) complexes is less than one proposal partial covalency in the bond of metal ligand. The octahedral geometry of these complexes is further supported by the value of υ_2/υ_1. In general, sterically bulk ligands give rise to relatively low Dq values [59].

The $\pi \rightarrow \pi$* and $\pi \rightarrow \pi$* transition show a red shift in dioxouranium(VI) complex (6). The band due to the intermolecular association and hydrogen bonding is absent. A non-ligand band at 23,600 cm^{-1} is assigned to the $^1\sum^+_g \rightarrow {}^3\pi_u$ transition of the UO$_2$ moiety [3]. In the present study of complex (6), it was observed that the ν_1 mode of the uranyl ion appears as weak intensity and ν_3 as strong intensity in the infrared spectrum (Table 5). The stretching and interaction force constant of the complex (6) was calculated from FT-IR spectrum to evaluate U–O bond [60, 61] as shown in Table 5. The data are quit close

Table 4 Electronic parameters of metal(II) complexes

Comp.[a]	υ_2/υ_1	B (cm^{-1})	β	10Dq (cm^{-1})	C	F_2	F_4
(4)	1.70	714	0.73	10,825	–	–	–
(5)	1.15	775	0.80	8520	2725	1160	77

[a]Numbers as given in Table 1

Table 5 Variation force constant (10^{-8} N/A°), U–O bond distances (A°) and frequencies (cm^{-1}) ν_1 and ν_3 of the UO_2^{2+} complex

ν_1	ν_3	F_{UO}	r_1	r_2	$(F^s_{U-O})_t$	r_t	$(F^s_{U-O})_o$	r_o	$(\nu_1^*)^c$	F^*_{U-O}	r_3
792	908	6.8052	1.7399	1.7177	6.0001	1.7643	5.8602	1.7690	824.4	6.2160	1.75774

[1,2] Internuclear distance U–O calculated by using Badger equation and Jones equation. [c]Symmetric stretching frequencies evaluated by using El-Sonbati equation. $(F^s_{U-O})_t$ is the true value of the force constant. $(F^s_{U-O})_a$ is the constant calculated with neglect of the ligand. F^*_{U-O} is the bond force constant which evaluated by using El-Sonbati equation. r_t is the internuclear distance U–O calculated by using the value of force constant. r_o is the internuclear distance U–O calculated by using the asymmetric stretching frequency with neglect of the ligands. r_3 is the internuclear distance U–O calculated by using the symmetric stretching frequency evaluated using El-Sonbati equation [56]

to the results reported earlier for other uranyl complexes [61–63].
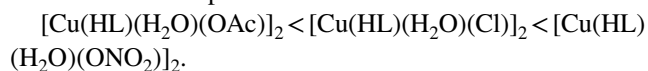
ESR spectra

The ESR spectra reveal the presence of a distorted tetragonal copper(II) complexes (1–3). This is evident from the trend of their respective $g_\parallel$ and $g_\perp$ values in all complexes $g_\parallel$ > $g_\perp$ > 2.0023 (Table 6). The electronic spectra of six-coordinate copper(II) complexes (1–3) consist of two transition energies (Table 6) and support binding of naphthalene and antipyrine ring imine nitrogen and carbonyl oxygen to the metal center, this beings the preferred nitrogen and oxygen atoms for coordination [64]. The energy of the d-d transition suggests distorted tetragonal copper(II) complexes [65] and follows the order:

$[Cu(HL)(H_2O)(ONO_2)]_2 < [Cu(HL)(H_2O)(Cl)]_2 < [Cu(HL)(H_2O)(OAc)]_2$.
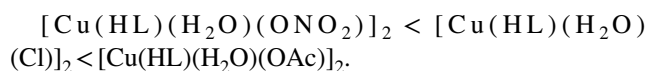
All complexes show ESR spectra with $g_\parallel$ > $g_\perp$ characteristic a tetragonally distorted octahedral geometry with the d_{x2-y2} orbital lowest in energy. The ESR parameters are calculated by the method of approximation suggested by Kneubuhl [65] and Garmen et al. [66], and the values are presented in Table 6. In all the complexes, the $g_\parallel$ < 2.3, which show that the complexes are largely covalent. Further, the values are consistent with the Cu–N and Cu–O bonded copper complexes [67, 68]. The $g_\parallel$ values for the complexes studied follow the order:

$[Cu(HL)(H_2O)(OAc)]_2 < [Cu(HL)(H_2O)(ONO_2)]_2 < [Cu(HL)(H_2O)(Cl)]_2$.
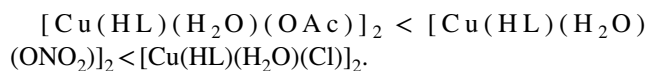
This appears to be the order of the strength of metal–anion interactions for chloride, nitrate and acetate [69]. The $g_{av.}$ values for the complexes studied follow the order:

$[Cu(HL)(H_2O)(OAc)]_2 < [Cu(HL)(H_2O)(Cl)]_2 < [Cu(HL)(H_2O)(ONO_2)]_2$.

The geometric parameter G, which is a measure of the exchange interaction between the copper centers in the compound using the equation:
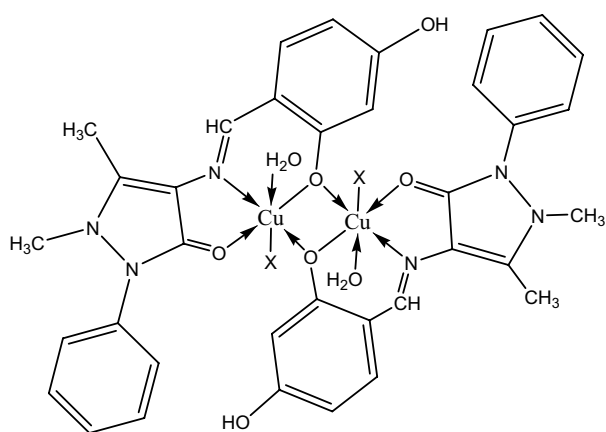
$G = g_\parallel - 2.0023/g_\perp - 2.0023$.

Accordingly, if G > 4, then the exchange may be negligible; however, if G < 4, the exchange interaction may be present, which is the case in the complexes under investigation. The G-values follow the order:

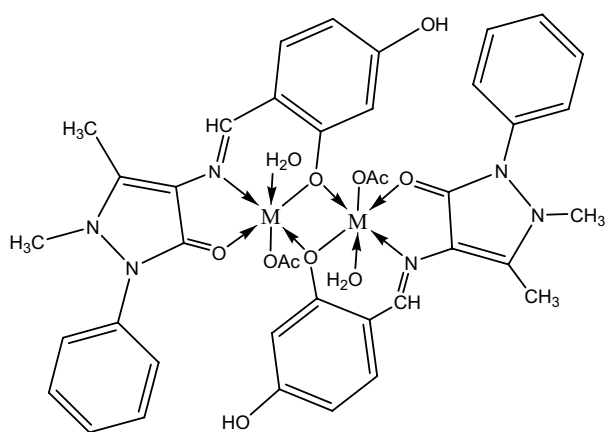$[Cu(HL)(H_2O)(OAc)]_2 < [Cu(HL)(H_2O)(ONO_2)]_2 < [Cu(HL)(H_2O)(Cl)]_2$.
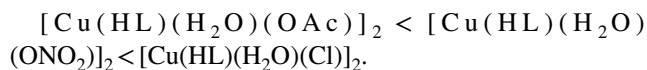
This is consistent with the order of the strength of metal–anion interaction. Our results are also in agreement with the respective positions of bonds and out-of-plane π bonds, respectively [70, 71]. These anions are given in the spectrochemical series [72]. The empirical factor (f) cm^{-1} is an index of tetragonal distorted around of Cu(II) ion [73].

The ESR parameters and the d-d transition energies are used to evaluate, the orbital reduction factor K by using the expression: $K^2 = K_{\parallel}^2 + 2 K_{\perp}^2/3$, where $K_\perp$ and $K_\parallel$ are the perpendicular and parallel components of the orbital reduction factor, respectively. In all case $K_\perp$ > $K_\parallel$, which is good evidence for the assumption of $^2B_{1g}$ as the ground state. For an ionic environment K = 1, and for a covalent environment K < 1, the lower the value of K, the greater is the covalent character. The values of $K_\parallel$ and $K_\perp$ for the complexes (Table 6) suggest marked amount of π-bonding in the planar environment whereas the π-contribution to the axial bonding is much smaller (see Table 6). Also, the in-plane σ-covalency parameter, α^2 was calculated [4, 74–77]. The α^2 values (Table 6) for these complexes indicate considerable covalency in the bonding between the copper(II) ion and the ligand Fig. 1.

The in-plane and out-plane π-bonding coefficients (β^2 and β_1^2) are dependent upon the values of d-d transitions.

Table 6 ESR parameters of Cu(II) complexes

Comp[a]	$g_\parallel$	$g_\perp$	g_{av}	G	α^2	ΔE_{xy}	ΔE_{xz}	$A_{\parallel}$	K^2	$K_{\parallel}$	$K_\perp$	β_1^2	β^2
1	2.15	2.06	2.090	2.56	0.40	15,267	23,256	75	0.65	0.34	0.81	0.85	2.03
2	2.17	2.06	2.097	2.91	0.42	14,641	23,640	72	0.67	037	0.82	0.88	1.96
3	2.18	2.05	2.093	3.73	0.41	15,039	24,628	160	071	0.40	0.86	0.98	1.73

[a]Numbers as given in Table 1

X = OAc⁻ (**1**); NO₃⁻(**2**) and Cl⁻(**3**)

M = Co(II) (**4**) and Mn(II) (**5**)

. 2CH₃COO⁻
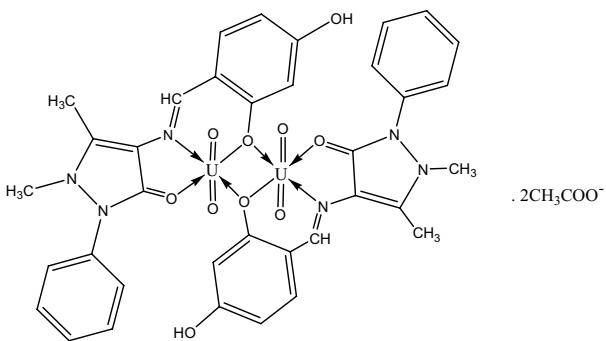
Fig. 1 Proposed structure of the complexes

Fig. 2 The XRD pattern of ligand (H₂L)

Fig. 3 The XRD pattern of complex (2)
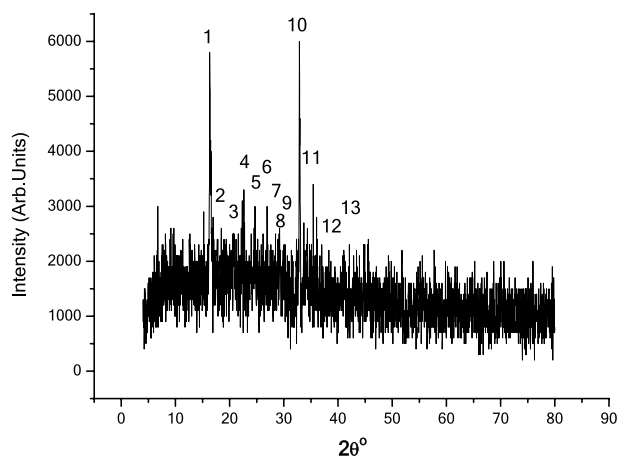
Fig. 4 The XRD pattern of complex (3)

Furthermore, α^2 and β_1^2 have value much less than 1 (the value for 100%, ionic bonding, this value decreasing with increasing covalent bonding), while $\beta^2 > 1$ (Table 6) assigns ionic character of the outer-of-plane π-bonding [4, 74–77].
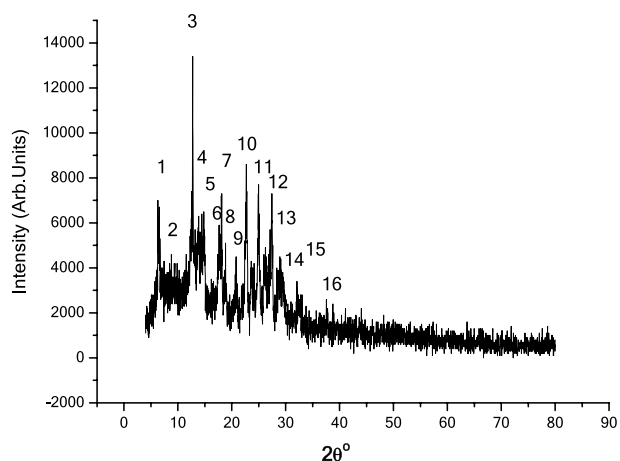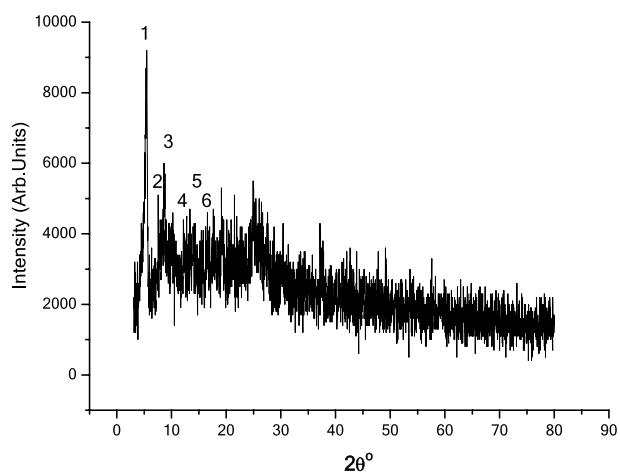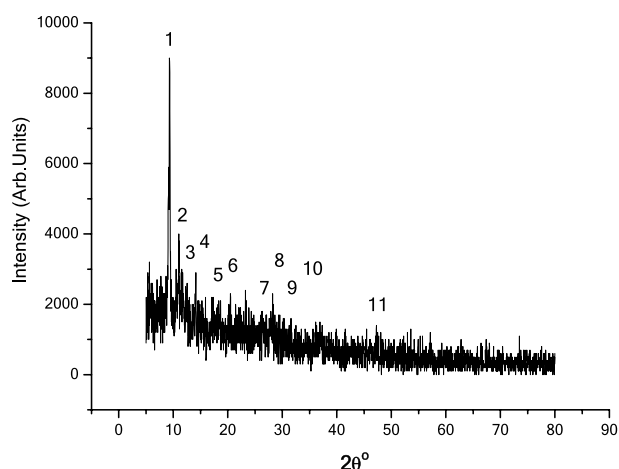
Fig. 5 The XRD pattern of complex (4)

Table 8 Crystallographic data for Cu(II) complex (**2**)

Sys*. Monoclinic S.G*

P2 a = 22.8600 Å b = 2.5030 Å c = 20.6310 Å

α = 90 ° β = 99.260 ° γ = 90 °

Peak no	$2\theta_{Obs.}$ (°)	$d_{Obs.}$ (Å)	$2\theta_{Calc.}$ (°)	$d_{Calc.}$ (Å)	(hkl)
1	5.359	16.4773	5.354	16.4927	$1\bar{1}01$
2	7.801	11.3239	7.831	11.2806	2200
3	8.648	10.2167	8.678	10.1814	.3002
4	13.480	6.5633	13.454	6.576	$4\bar{3}02$
5	14.063	6.2925	14.093	6.2792	$5\bar{2}03$
6	15.707	5.6374	15.698	5.6406	$6\bar{4}00$

Sys.*: System

S. G*.: Space group

Table 7 Crystallographic data for H_2L ligand

Sys*. Triclinic S.G*. P1
a = 14.8120 Å b = 9.8390 Å c = 6.2540 Å
α = 86.7 ° β = 106.12 ° γ = 106.05 °

Peak no	$2\theta_{Obs.}$ (°)	$d_{Obs.}$ (Å)	$2\theta_{Calc.}$ (°)	$d_{Calc.}$ (Å)	(hkl)
1	6.4509	13.6906	6.4525	13.6872	$\bar{1}00$
2	9.3855	9.6928	9.3549	9.4462	010
3	12.7219	6.9527	12.7406	6.9425	$\bar{1}10$
4	13.7697	6.4259	13.7513	6.4344	$2\bar{1}0$
5	14.7358	6.0067	14.7446	6.0031	001
6	17.5900	5.0379	17.5781	5.0413	$\bar{2}11$
7	17.9807	4.9293	17.9734	4.9313	$\bar{1}1\bar{1}$
8	18.7861	4.7198	18.7730	4.7231	$0\bar{2}0$
9	20.7566	4.27596	20.7569	4.2759	$\bar{2}1\bar{1}$
10	22.6846	3.9167	22.7036	3.9135	$\bar{2}21$
11	23.6991	3.7513	23.7079	3.7499	$0\bar{2}\bar{1}$
12	24.9712	3.563	24.9989	3.5591	$\bar{3}1\bar{1}$
13	26.2333	3.3944	26.2009	3.3985	$\bar{4}01$
14	27.3885	3.2538	27.3842	3.2543	121
15	29.0230	3.0741	29.0170	3.0748	$\bar{2}02$
16	37.6843	2.3851	37.6984	2.3842	$\bar{6}21$

Sys.*: System

S. G*.: Space group

Table 9 Crystallographic data for Cu(II) complex (3)

Sys*. Monoclinic S.G* P21
a = 9.1800 Å b = 6.9650 Å c = 8.4940 Å
α = 90 ° β = 110.74° γ = 90 °

Peak no	$2\theta_{Obs.}$ (°)	$d_{Obs.}$ (Å)	$2\theta_{Calc.}$ (°)	$d_{Calc.}$ (Å)	(hkl)
1	16.3987	5.4011	16.4000	5.4007	$\bar{1}10$
2	17.6861	5.0108	17.7055	5.0053	101
3	20.7352	4.2803	20.7087	4.2857	$\bar{2}00$
4	22.4120	3.9637	22.3922	3.9672	002
5	24.5764	3.6193	24.5708	3.6201	$\bar{2}02$
6	26.8610	3.3165	26.8984	3.3119	201
7	27.6699	3.2213	27.6607	3.2223	$\bar{1}20$
8	29.1934	3.0566	29.2058	3.0553	$\bar{3}01$
9	29.8934	2.9866	29.8563	2.9902	211
10	32.8891	2.7211	32.8677	2.7228	$\bar{2}03$
11	34.2704	2.6145	34.2629	2.6150	022
12	39.4801	2.2807	39.4910	2.2801	$\bar{3}13$
13	41.1052	2.1942	41.1357	2.1926	$\bar{1}23$

Sys.*: System

S. G*.: Space group

X-Ray diffraction analysis

The X-ray diffraction analysis is used for determining the structure of H_2L and its complexes **2, 3** and **5** are shown in Figs. 2, 3, 4, 5. Many diffraction peaks were observed which indicate the polycrystalline phase.

The a, b, c, α, β and γ values of the estimated lattice parameters, inter-planar spacing (d) values and Miller indices hkl values of H_2L ligand and its complexes (**2, 3** and **5**) are determined by using CHEKCELL program [78]. The values of estimated lattice parameters (a, b, c, α, β and γ), d and hkl for ligand (H_2L) and its complexes (**2, 3** and **5**) are listed in Tables 7, 8, 9, 10, respectively.

The results show that many diffraction peaks were observed which indicate the polycrystalline phase and the ligand (H_2L) is polycrystalline with triclinic crystal system with space group P1. The complexes (**2 and 3**) are

Table 10 Crystallographic data for Mn(II) complex (**5**)

Sys*. Triclinic S.G*. P1
a = 9.9400 Å b = 8.9840 Å c = 10.7390 Å
α = 65.31° β = 103.91° γ = 104.64 °

Peak no	$2\theta_{Obs.}$ (°)	$d_{Obs.}$ (Å)	$2\theta_{Calc.}$ (°)	$d_{Calc.}$ (Å)	(hkl)
1	9.2764	9.5259	9.2973	9.5046	$\overline{1}00$
2	10.9984	8.0380	10.9938	8.0414	010
3	12.3907	7.1378	12.3891	7.1387	$\overline{1}11$
4	14.0623	6.2928	14.0398	6.3029	101
5	18.3698	4.8258	18.3866	4.8214	002
6	20.4477	4.3398	20.4317	4.3432	021
7	26.4259	3.3701	26.4286	3.3697	$\overline{2}20$
8	27.9094	3.1942	27.9091	3.1942	$\overline{2}13$
9	29.3955	3.036	29.3950	3.0361	113
10	31.3876	2.8477	31.3990	2.8467	032
11	47.3018	1.9202	47.2977	2.135	$\overline{3}15$

Sys.*: System

S. G*.: Space group

polycrystalline with monoclinic crystal system with space group P2 and P21, respectively. Complex (**5**) is polycrystalline with triclinic crystal system with space group P1.

Thermogravimetric analysis data

The loss of mass percentages in the temperature range 30–800 °C of thermogravimetric analyses data of the H_2L ligand and its complexes of Cu(II), Co(II), Mn(II) and UO_2(II) are listed in Table 11 and presented in Fig. 6.

The TG curve of the ligand (H_2L) shows decomposition at 30 °C in four stages. Weight loss of the first step at the temperature range 30–127 °C found 14.1% (calcd. 14.2%) due to loss of C_2H_6O. The second stage is found loss of C_2HN (found 12.38%; calcd. 12.07%) (127–259 °C). The third stage is found to loss of $C_7H_5N_2O$ (found 41.1%; calcd. 41.18%) (259–479.87 °C). The final stage at the temperature range 479.87–768 °C due to loss of C_7H_5O (found 32.35%; calcd. 32.5%).

The TGA curve of the complex [Cu(HL)(H_2O)(OAc)]_2(**1**) decomposed in two steps, the first step occurred at temperature between 30 and 284 °C due to the loss of $CH_3COO + H_2O + C_2H_6$ (found 22.5%; calcd. 23.1%) [24, 79]. The second step at 284–800 °C which related to loss $C_8H_{10}N_3O_2$ (found 39.4%; calcd. 38.9%) and the residue is CuO with eight carbon atoms (found 38%; calcd 38%).

The TGA curve of the complex [Cu(HL)(H_2O)(ONO_2)]_2 (**2**) decomposed in four steps, the first step at temperature range 30–130 °C was found loss of $HNO_3 + H_2O$ (found 17.1%; calcd.17.4%). The second stage at 130–247 °C

corresponded to the loss of $C_2H_6N_2$ (found 15.1%; calcd. 15.3%). The third step between 247 and 439 °C was corresponding to the loss of $C_4H_4NO_2$ (found 18.8%; calcd. 18.3%). The final step at 439–785 °C due to losing of C_6H_5 (found 16.8%; calcd. 16.7%). CuO is residue and six carbon atoms (found 32.2% and calcd. 32.6%).

The TGA curve of the complex [Cu(HL)(H_2O)(Cl)]_2(**3**) decomposed in four steps, the first step at temperature ranging between 30 and 124 °C attributed to the loss of HCl molecules (found 8.4%; calcd. 8.3%). The second stage at 124–280 °C was related to loss of one coordinated water molecule and part of the complex $C_3H_6N_2$(found 20.2%; calcd. 20%), the third stage due to the loss of C_3HNO as a part of the complex (found 14.9%; calcd. 15.3%) (280–450 °C) and the fourth stage at 450–766 °C due to the loss of C_4H_8O as a part of the complex (found 16.8%; calcd. 16.4%). CuO and eight carbon atoms is a residue (found 39.7%; calcd. 40%).

The thermal decomposition of [Co(HL)(H_2O)(OAc)]_2(**4**) showed two TG steps. The first step is loss of one water molecule and acetate group (found 16.7%;calcd. 16.8%) at temperature range 30–241.6 °C. The second step is loss of $C_{12}H_{16}N_3O_2$ (found 50.8%; calcd. 51%) at 241.6–800 °C. CoO and six carbon atoms are a residue (found 32.5%; calcd. 32.1%).

The TG curve of [Mn(HL)(H_2O)(OAc)]_2 (**5**) degraded in three steps. The first step started at 30–60 °C represents the loss of one molecule of water (found 3.8%; calcd. 3.9%). The second step due to the loss of coordinated acetate group, further decomposition of methyl group (CH_3) at 60–238 °C (found 16.2%; calcd. 16.3%) and the third stage, represented the loss of $C_9H_{13}N_3O_2$ at 238–780 °C (found 43.2%; calcd. 43%) leaving MnO as a residue with eight carbon atoms (found 36.8%; calcd. 36.8%).

The TG curve of {[UO_2(HL)]_2. 2(OAc)} (**6**) decomposes in four steps. The first step starts at 30–237 °C represents the loss of coordinated acetate group (found 8.7%; calcd. 9.0%), the second stage represented the loss of C_2H_6 at temperature 237–322 °C and the loss represented by (found 5%; calcd. 4.6%), the third stage at temperature 322–468 °C represented loss of $C_3H_2N_3O_2$ and the results were (found 17.5%; calcd. 17.2%) and the fourth stage represented loss of C_6H_8O at 468–796 °C and the results were represented as (found 14.4%; calcd. 14.7%). The remaining of decomposition was UO_2 with seven carbons atoms.

Kinetic studies

The kinetic parameters such as the thermal activation energy of decomposition (E_a), enthalpy (ΔH^*), entropy (ΔS^*) and Gibbs free energy change of the decomposition (ΔG^*) are evaluated graphically by employing the Coast–Redfern and Horowitz–Metzger methods [80, 81].

Table 11 TGA thermal data of the ligand (H_2L) and complexes

Compound[a]	Temperature range (°C)	TG weight loss %		Assignments
		Found	Calc	
H_2L	30–127	14.1	14.2	C_2H_6O
	127–259	12.38	12.07	C_2HN
	259–479.87	41.1	41.18	$C_7H_5N_2O$
	479.87–768	32.35	32.5	C_7H_5O
(1)	30–284	22.5	23.1	$CH_3COO + H_2O + C_2H_6$
	284–800	39.4	38.9	$C_8H_{10}N_3O_2$
	Remain	38	38	$CuO + 8C$
(2)	30–130	17.1	17.4	$HNO_3 + H_2O$
	130–247	15.1	15.3	$C_2H_6N_2$
	247–439	18.8	18.3	$C_4H_4NO_2$
	439–785	16.8	16.7	C_6H_5
	Remain	32.2	32.6	$CuO + 6C$
(3)	30–124	8.4	8.3	HCl
	124–280	20.2	20	$C_3H_6N_2 + H_2O$
	280–450	14.9	15.3	C_3HNO
	450–766	16.8	16.4	C_4H_8O
	Remain	39.7	40	$CuO + 8C$
(4)	30–241.6	16.7	16.8	$H_2O + CH_3COO$
	241.6–800	50.8	51	$C_{12}H_{16}N_3O_2$
	Remain	32.5	32.1	$CoO + 6C$
(5)	30–60	3.8	3.9	H_2O
	60–238	16.2	16.3	$CH_3 + CH_3COO$
	238–780	43.2	43	$C_9H_{13}N_3O2$
	Remain	36.8	36.8	$MnO + 8C$
(6)	30–237	8.7	9	CH_3COO
	237–322	5	4.6	C_2H_6
	322–468	17.5	17.2	$C_3H_2N_3O_2$
	468–796	14.4	14.7	C_6H_8O
	Remain	54.4	54.4	$UO_2 + 7C$

[a]Numbers as given in Table 1

Coast–Redfern equation

The Coast–Redfern equation, which is a typical integral method, can represent as:

$$\int_0^a \frac{dx}{(1-\alpha)^n} = \frac{A}{\varphi} \int_{T_1}^{T_2} \exp\left(-\frac{E_a}{RT}\right) dt \tag{1}$$

For convenience of integration, the lower limit T_1 usually taken as zero. This equation on integration gives:

$$\ln\left[-\frac{\ln(1-\alpha)}{T^2}\right] = -\frac{E_a}{RT} + \ln\left[\frac{AR}{\varphi E_a}\right] \tag{2}$$

A plot of left-hand side (LHS) against 1/T was drawn (Fig. S12). E_a is the thermal activation energy of decomposition. The entropy of activation calculated by using the equation:

$$\Delta S^* = 2.303\left[\log\left(\frac{Ah}{k_B T_s}\right)\right] R \tag{3}$$

where k_B is the Boltzmann constant, h is the Plank's constant and T_s is the TG peak temperature.

Horowitz–Metzger equation

The Horowitz–Metzger equation is an illustrative of the approximation methods. These authors derived the relation:

$$\log\left[\frac{1-(1-\alpha)^{1-n}}{1-n}\right] = \frac{E_a\theta}{2.303RT_S^2} \; for \, n \neq 1 \tag{4}$$

when $n = 1$, the LHS of Eq. (4) would be log[-log(1-α)] (Fig. S13). For a first-order kinetic process, the Horowitz–Metzger equation may write in the form:

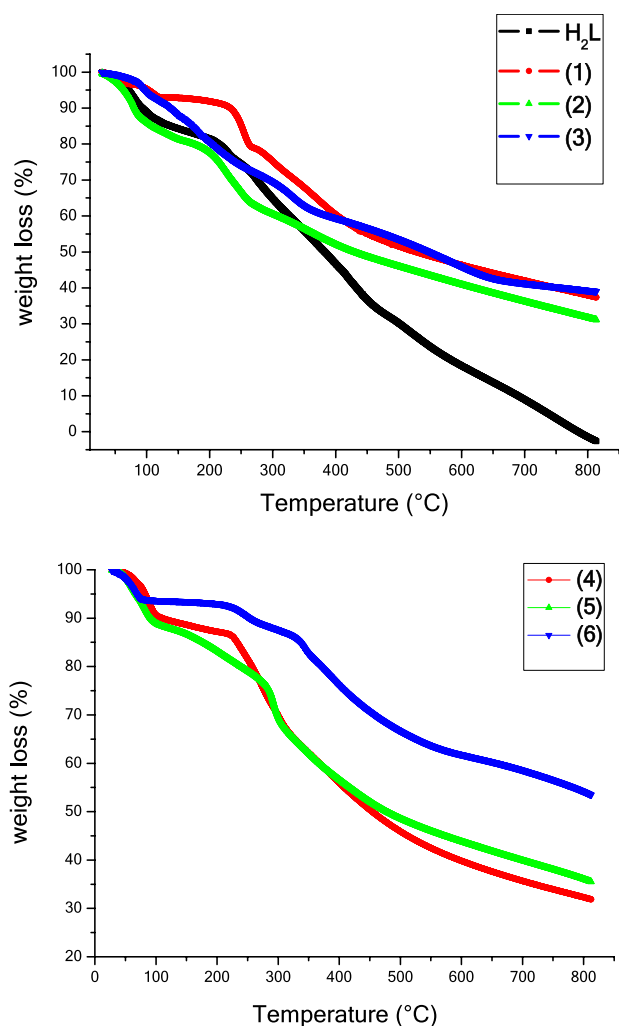$$\Delta H^* = E_a - RT \tag{7}$$

$$\Delta G^* = \Delta H^* - T\Delta S^* \tag{8}$$

The activation energy (E_a), entropy (ΔS), Gibbs free energy (ΔG) and enthalpy (ΔH) values of the decomposition of the ligand (H_2L) and its complexes are determined graphically and listed in Table 12 using Horowitz–Metzger and Coast–Redfern methods [80, 81]. From the slopes in Figs. S12 and S13 of the ligand (H_2L) and complexes, E_a activation energy (kJ mol^{-1}) can be calculated. From the thermal activation energy values of decomposition for ligand (H_2L) and complexes, it was found that the E_a activation energy value of the $UO_2(II)$ complex (6) is higher than the other complexes, indicating that the $UO_2(II)$ complex (6) is the most stable complex [76, 77, 82].

From the results obtained, the following remarks can be pointed out:

(1) The high values of the thermal activation energy of decomposition (E_a) of the complexes reveal the high stability of such chelates due to their covalent bond character.

(2) From the values of the E_a of the ligand (H_2L) and its complexes (1–6), it was found that the E_a value for the complex (6) is higher compared to the other complexes.

(3) The Gibbs free energies of decomposition (ΔG^*) for the ligand (H_2L) and its complexes (1–6) are positive values which indicate that the processes are non-spontaneous.

(4) The negative values of ΔS^* for the decomposition steps in the ligand (H_2L) and its complexes (1–6) indicate more ordered activated complex than the reactants or the reaction is slow.

(5) From the relation between the thermal activation energy of decomposition (E_a) by employing the Coast–Redfern and Horowitz–Metzger methods and representative Pascal constants of Cu(II) complexes, it is observed that the E_a values of the formed complexes increases in the order Cl$^- >$ OCOCH$_3^-$. Our results are also in agreement with the respective positions of these anions as given in the representative Pascal constants [83]. This is consistent with the order of the strength of metal–anion interactions, i.e., chloride > acetate. Our results are also in agreement with the respective positions of these anions as given in the representative Pascal constants [83].

Fig. 6 TG curves of the ligand (H_2L) and its polymer complexes (1-6)

$$\log\left[\log\left(\frac{W_\alpha}{W_\gamma}\right)\right] = \frac{E_a\theta}{2.303RT_S^2} - \log 2.303 \tag{5}$$

where $\theta = T - T_s$, $w_\gamma = w_\alpha - w$, $w_\alpha =$ mass loss at the completion reaction; $w =$ mass loss up to time t. The plot of log [log (w_α / w_γ)] *vs.* θ was drawn and found to be linear from the slope of which E_a was calculated. The pre-exponential factor, A, calculated from equation:

$$\frac{E_a}{RT_S^2} = \frac{A}{\left[\varphi \exp\left(\frac{-E_a}{RT_S}\right)\right]} \tag{6}$$

The entropy of activation, ΔS^*, is calculated from Eq. (3). The enthalpy activation, ΔH^*, and Gibbs free energy, ΔG^*, calculated from:

Table 12 Thermodynamic data of the thermal decomposition of ligand (H$_2$L) and its complexes

Compound[a]	Decomposition temperature (°C)	Method	Thermodynamic parameters				Correlation coefficient
			E_a(kJ mol^{-1})	ΔS^*(J mol^{-1} K^{-1})	ΔH^*(kJ mol^{-1})	ΔG^*(kJ mol^{-1})	
H$_2$L	30–112	CR	59.7	−119	56.8	97.7	0.97184
		HM	66.6	−89.9	63.7	94.7	0.96318
(1)	223–611	CR	17.6	−285	11.8	209	0.9908
		HM	29.7	−264	24.0	206	0.97941
(2)	175–268	CR	58.6	−121	54.5	114	0.95545
		HM	75.0	−140	70.9	140	0.98704
(3)	30–90	CR	88.1	−58.1	85.3	105	0.96954
		HM	76.8	−51.0	74.0	91.0	0.97837
(4)	218–574	CR	24.2	−272	18.6	201	0.98195
		HM	33.2	−256	27.6	199	0.98832
(5)	101–284	CR	30.3	−239	26.4	138	0.99607
		HM	38.3	−213	34.4	134	0.98919
(6)	30–70	CR	98.8	17.8	96.1	90.4	0.97027
		HM	104	42.8	101	87.2	0.96374

[a]Numbers as given in Table 1

Table 13 Antibacterial activities of the ligand (H$_2$L) and its complexes in comparison with benzylpenicillin (penicillin G) as a standard drug. The diameter of zones of inhibition (mm)

Compounds[a]	Concentration, µg/mL	Gram-positive bacteria		Gram-negative bacteria		
		Bacillus cereus	*Staphylococcus aureus*	*Escherichia coli*	*Klebsiellapneumoniae*	*Pseudomonas* sp.
H$_2$L	50	−ve	−ve	−ve	−ve	−ve
	100	9±0	−ve	−ve	−ve	−ve
	150	12±0	−ve	11±0	−ve	11±0
1	50	−ve	−ve	−ve	−ve	−ve
	100	10±0	−ve	−ve	−ve	−ve
	150	13±0	−ve	−ve	−ve	−ve
2	50	−ve	−ve	−ve	−ve	−ve
	100	10±0	−ve	10±±0.06	−ve	10±0
	150	13±0	−ve	13±±0.06	−ve	13±0
3	50	10±0	19±0	11±±0.06	17±0.03	11±0
	100	13±0	22±0	13±0.14	20±0	13±0.14
	150	15±0	25±0.03	15±0.14	24±0.06	15±0.14
4	50	17±0.03	10±0	−ve	−ve	−ve
	100	20±0	13±0	−ve	−ve	−ve
	150	24±0.06	15±0	−ve	−ve	−ve
5	50	11±0	11±0	−ve	−ve	−ve
	100	14±0	14±0	10±±0.06	−ve	10±0.03
	150	16±0	16±0	13±±0.06	−ve	13±±0.03
6	50	10±0	−ve	−ve	−ve	−ve
	100	13±0	−ve	−ve	−ve	−ve
	150	15±0	−ve	−ve	−ve	−ve
Penicillin G	50	9±0	10±0	33±0.03	−ve	11±0
	100	11±0.03	11±0	37±0.03	−ve	14±0.06
	150	13±0	16±0.03	39±0	−ve	20±0

[a]Numbers as given in Table 1

Table 14 Antifungal activities of ligand (H₂L) and its complexes in comparison with miconazole as a standard drug. The diameter of zones of inhibition (mm)

Compounds[a]	Concentration, μg/mL	Fungi		
		Aspergillus niger	Fusarium oxysporum	Candida albicans
H₂L	50	−ve	−ve	−ve
	100	−ve	−ve	−ve
	150	−ve	−ve	−ve
1	50	−ve	−ve	−ve
	100	−ve	−ve	11 ± 0
	150	−ve	−ve	13 ± 0
2	50	−ve	−ve	−ve
	100	−ve	−ve	−ve
	150	−ve	−ve	−ve
3	50	−ve	−ve	−ve
	100	−ve	−ve	−ve
	150	−ve	−ve	11 ± 0.14
4	50	−ve	−ve	−ve
	100	−ve	−ve	−ve
	150	−ve	−ve	−ve
5	50	−ve	−ve	−ve
	100	−ve	−ve	11 ± 0
	150	−ve	−ve	15 ± 0
6	50	−ve	−ve	−ve
	100	−ve	−ve	−ve
	150	−ve	−ve	−ve
Miconazole	50	10 ± 0.06	8 ± 0.14	11 ± 0
	100	13 ± 0.14	10 ± 0.14	13 ± 0
	150	18 ± 0.14	13 ± 0.14	16 ± 0

[a]Numbers as given in Table 1

Antimicrobial activity of H₂L ligand and its complexes

Antimicrobial activity of H₂L ligand and its complexes were tested against *Staphylococcus aureus* and *Bacillus cereus* as gram-positive bacteria and *Klebsiella pneumoniae, Escherichia coli* and *Pseudomonas* sp.) as gram-negative bacteria as well as antifungal activities were determined against *Fusarium oxysporum, Aspergillus niger* and *Candida albicans* and the results are listed in Tables 13 and 14.

H₂L ligand and its complexes (**1–6**) have antibacterial activity against *Bacillus cereus* where complexes (**3–6**) have higher antibacterial activity than penicillin G which is used as the antibacterial standard drug against *Bacillus cereus*. The ligand (H₂L) and its complexes (**1, 2 and 6**) have no antibacterial activity against *S. aureus* while the complexes (**3–5**) have high antibacterial activity against *S. aureus*.

H₂L ligand and its complexes (**1, 2 and 6**) have no antibacterial activity against *Staphylococcus aureus* while the complexes (**3–5**) have high antibacterial activity against *Staphylococcus aureus*.

The ligand has antibacterial activity against *E.coli*(inhibition zone = 11 mm at concentration = 150 μg/mL). The complexes (**1, 4 and 6**) have no antibacterial activity against *E. coli* while the complexes (**2, 3 and 5**) have high antibacterial activity against *E. coli*.

H₂L ligand and its complex have no antibacterial activities against *Klebsiella pneumoniae* except complex (**3**). The complex (**3**) is more active than the antibacterial standard drug (penicillin G) against *Klebsiella pneumoniae*. The complex (**3**) showed very good antibacterial activity in comparison with penicillin G. The compounds which contain nitrogen atoms and the complex which contain chlorine atoms such as Schiff base and azodye compounds usually showed antibacterial activities [25]. The outcomes showed that the complex (**3**) is very good antibacterial agents against *Staphylococcus aureus* and *Klebsiella pneumoniae* (Table 13).

The complexes (**1, 4 and 6**) have no antibacterial activity against *Pseudomonas* sp. The complexes (**2, 3 and 5**) have antibacterial activity against *Pseudomonas* sp. H₂L has antibacterial activity against *Pseudomonas*

sp. (inhibition zones = 11 mm at concentration = 100 µg/mL and 14 mm at concentration = 150 µg/mL) and the ligand has antibacterial activity against *Pseudomonas* sp.(inhibition zone = 11 mm at concentration = and 150 µg/mL) as listed in Table 13. The complex (2) has antibacterial activity against *Pseudomonas* sp. (inhibition zones = 10 mm at concentration = 100 µg/mL and 13 mm at concentration = 150 µg/mL). The complex (3) has antibacterial activity against *Pseudomonas* sp. (inhibition zones = 11 mm at concentration = 50 µg/mL, 13 mm at concentration = 100 µg/mL and 15 mm at

concentration = 150 µg/mL). The complex (5) has antibacterial activity against *Pseudomonas* sp. (the inhibition zones = 10 and 13 mm at concentrations = 100 and 150 µg/mL, respectively).

The results of antifungal activity of H_2L and complexes (1–6) are studied against *Candida albicans, Fusarium oxysporum* and *Aspergillus niger* and shown in Table 14. The ligand H_2L and all complexes have no antifungal activities against *Fusarium oxysporum* and *Aspergillus niger*.

(a)   **(b)**
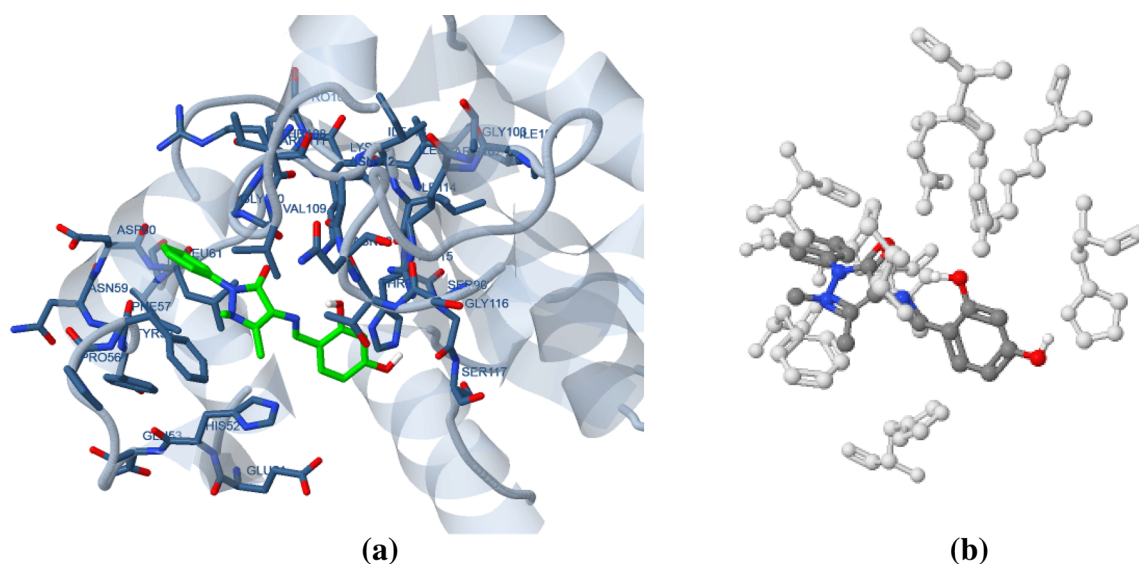
Fig.7 The ligand (H_2L) (green in (a) and gray in (b)) in interaction with receptor of *Staphylococcus aureus* (3q8u)

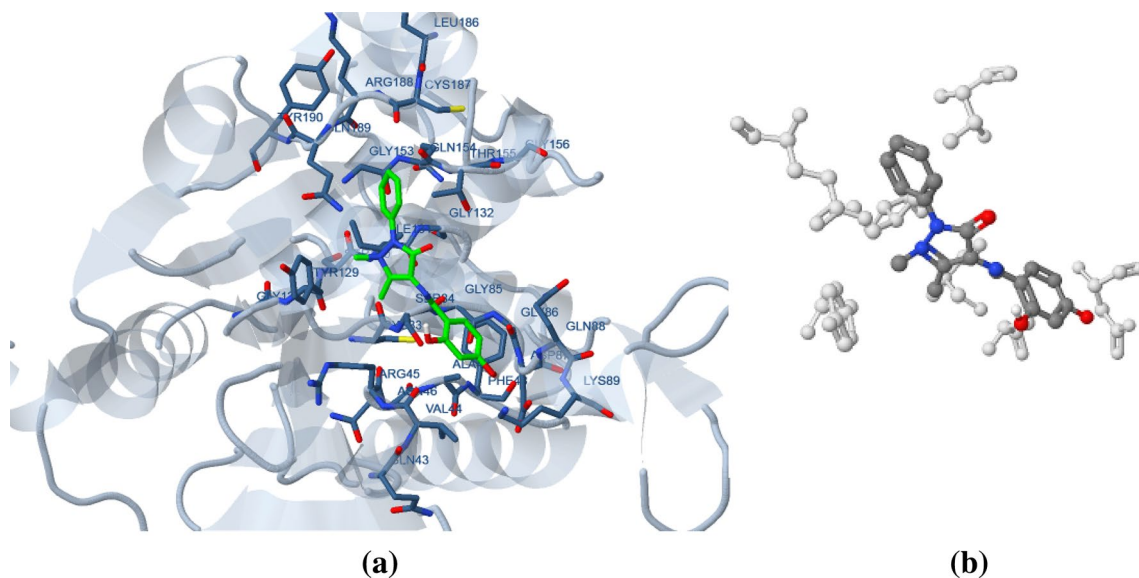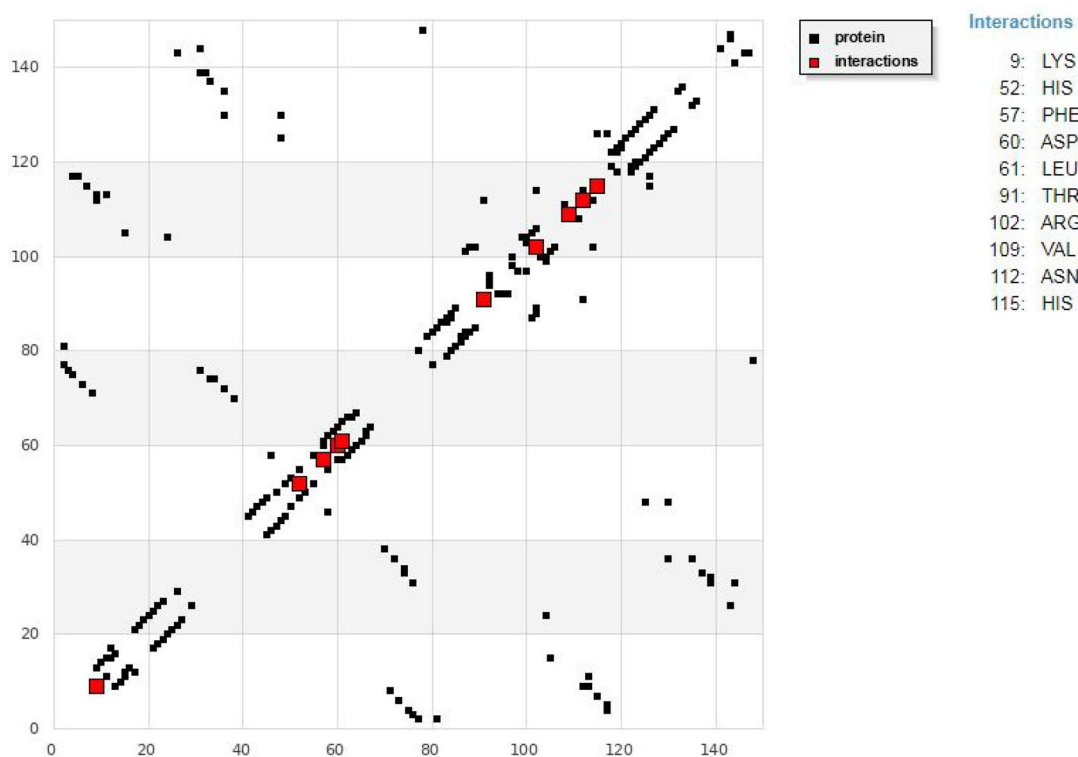
(a)   **(b)**

Fig. 8 The ligand (H_2L) (green in (a) and gray in (b)) in interaction with receptor of *Escherichia coli* (3t88)

Table 15 The values of energy obtained in docking calculations of the ligand (H₂L) with receptors of *Staphylococcus aureus* (3q8u) and *Escherichia coli* (3t88)

Receptors	Est. Free Energy of binding (kcal/mol)	Est. inhibition constant (Kᵢ) (µM)	vdW + bond + desolv energy (kcal/mol)	Electrostatic energy (kcal/mol)	Total intercooled energy (kcal/mol)	Interact surface
3q8u	− 5.89	48.26	− 6.70	− 0.20	− 6.90	856.747
3t88	− 5.00	217.90	− 5.98	− 0.06	− 6.04	672.462

Fig. 9 HB plot of interaction between the ligand (H₂L) and receptor of *Staphylococcus aureus* (3q8u)

It was found that the H₂L and complexes **(1–6)** have no anticandidal activity against *Candida albicans* at concentration = 50 µg/mL. Also, the ligand and its complexes **(2, 4** and **6)** have no anticandidal activity against *Candida albicans* at all concentrations. The complex **(1)** has anticandidal activity against *Candida albicans* (inhibition zones = 11 mm at concentration = 100 µg/mL and 13 mm at mm at concentration = 150 µg/mL). The complex **(3)** has anticandidal activity against *Candida albicans* (inhibition zone = 11 mm at concentration = 150 µg/mL). The complex **(5)** has anticandidal activity against *Candida albicans* (inhibition zones = 11 and 15 mm at concentrations = 100 and 150 µg/mL, respectively).

Molecular docking

The molecular docking of the ligand (H₂L) revealed the interacting active residues with receptors, which was endorsed to interlink with phytochemical by the energies and interact surface area size [32]. The present results obtained from data showed that the molecular interactions of ligand with *Staphylococcus aureus* (3q8u) and *Escherichia coli* (3t88) as shown in Figs. 7 and 8 are mentioned in Table 15, which indicates specific bonds and atoms involved in the docking.

The results of the molecular docking between the H₂L ligand and the receptors of *Staphylococcus aureus* (3q8u) and *Escherichia coli* (3t88) showed a possible arrangement between the receptors (*S. aureus* (3q8u) and *E. coli* (3t88)) and the ligand. From Figs. 7 and 8 and the calculated energy is listed in Table 15 showed a favorable interaction between
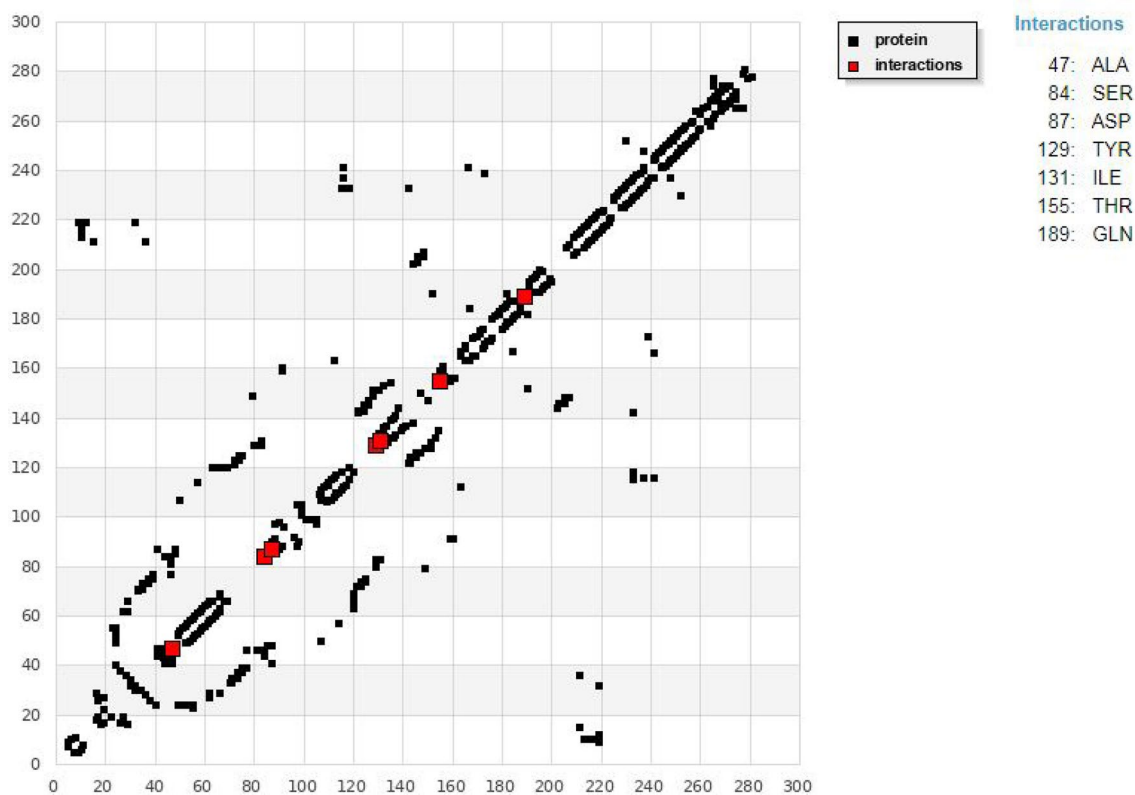
Fig. 10 HB plot of interaction between the ligand (H₂L) and receptor of *Escherichia coli* (3t88)

the receptors (*S. aureus* (3q8u) and *E. coli* (3t88)) and the ligand. Figures 9 and 10 show curves of HB of docking with ligand. Figures 11 and 12 show curves of 2D of docking with ligand. The ligand showed similar interaction results with *Staphylococcus aureus* (3q8u) and *Escherichia coli* (3t88) receptors.

Tafel polarization methods

Polarization tests were carried out to study the inhibition efficiency of the prepared ligand (**H₂L**) against the corrosion of carbon steel in HCl (2 M) solution give information concerning the kinetics of the anodic and cathodic reactions. Figure 13 give the polarization habit of C-steel electrode in acidic medium without and with different doses of H₂L as inhibitor. Figure 13 illustrates affected both the anodic and cathodic reactions by appending of investigated compound (H₂L), and the % IE rise as the dose of inhibitor rise, but the cathodic is more protective, indication by appending of compound (H₂L) lower the anodic C-steel liquefaction and also prevent the cathodic reactions. Therefore, investigated compound (H₂L) is play as mixed kind inhibitor.

The outcome data in Table 16 give that the current corrosion density lower obviously after the appending of

inhibitors and % IE rise with rising the dose of inhibitor. The %IE_p was measured utilizing as the following:

$$\%IE_p = \left[\frac{i^o corr - i\,corr}{i^o corr} \right]$$

where i_{corr} and i^o_{corr} are the inhibited and uninhibited corrosion current densities, severally.

It is illustrated from Table 5 the adsorbed inhibitor act by plain blocking of the active center for both anodic and cathodic. In other words, the inhibitor adsorbed lower the surface area for corrosion without impact the C-steel corrosion mechanism and only causes inactivation of a part of the surface with respect to corrosive solution [84].

EIS technique

EIS is strength test in the research of corrosion [85–88]. Figure 14 gives Nyquist (a) and Bode (b) curves shown at open-circuit potential both in attendance and lack of improving doses of investigated compound (H₂L). The rise in the area of the capacitive loop with the appending of compound (H₂L) illustrated that a barrier stepwise forms on the alloy surface.

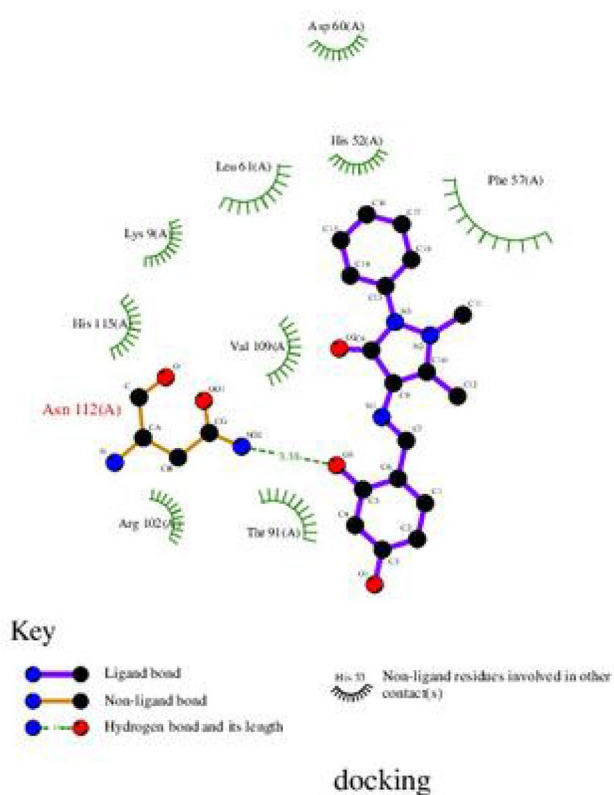The Nyquist curves do not give semicircles perfect as hope-for from the theory of EIS. The declination from

Fig.11 2D plot of interaction between the ligand (H$_2$L) and receptor of *Staphylococcus aureus* (3q8u)

Fig. 12 2D plot of interaction between the ligand (H$_2$L) and receptor of *Escherichia coli* (3t88)

semicircle ideal was stepwise imputed to the dispersion frequency [89]. EIS spectra of the organic appending were measure utilized the equivalent circuit, Fig. 15, given a single reaction charge transfer and follow well with our experimental outcome. The CPE is interring in the circuit equivalent of a pure capacitor double layer to obtain a more correct fit [90]. The double-layer capacitance, C$_{dl}$, is measured as equation:

$$C_{dl} = \frac{Y_o \omega^{n-1}}{\sin\left[n\left(\frac{\pi}{2}\right)\right]}$$

where Y$_o$ = CPE magnitude, $\omega = 2\pi f_{max}$, f$_{max}$ = frequency of imaginary component of the impedance is maximal and n = factor an parameter exactly that utilized among 0.50 and 1.0.

After authorization the plot of the Nyquist curve, it is noted that the diagrams nearly by a single semicircles capacitive, giving that the corrosion mechanism was widely charged-transfer command [91, 92]. The mostly shape of the plots is very like for all solutions (without and with inhibitors at unlike flooding times) lead to corrosion process no change [93]. From EIS
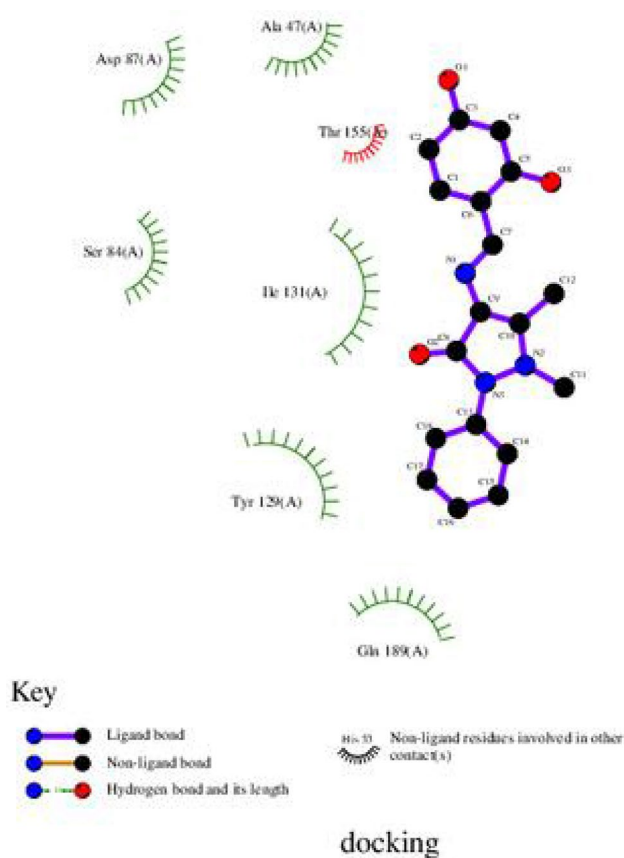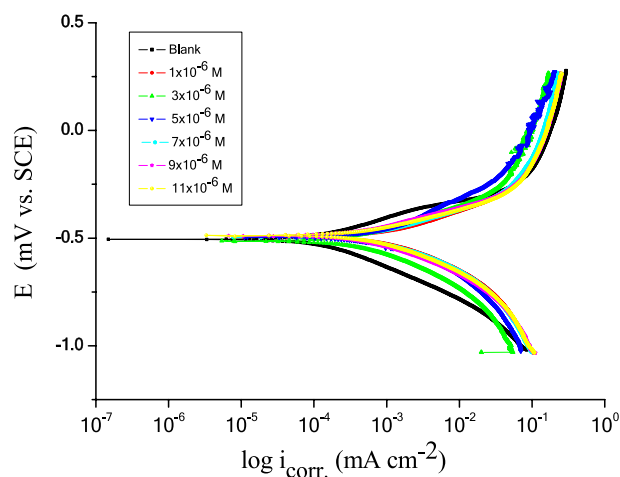

Fig. 13 Potentiodynamic polarization curves for the corrosion of C-steel in 2 M HCl attendance and lack of unlike dose of compound (H$_2$L) at 30 ± 0.1 °C

value (Table 17), we contain that the data of R$_{ct}$ rise with improving the dose of the inhibitor. The data of R$_{ct}$ in acidic medium rise with attendance of inhibitor.

Table 16 Effect of dose of the investigated compound (H₂L) on the free corrosion potential ($E_{corr.}$), ($i_{corr.}$), (β_a & β_c), (θ) and (% IE) for C-steel in 2 MHCl at 30 ± 0.1 °C

Compound	Conc. (M)	$-E_{corr \times 10^{-3}}$ (mV vs. SCE)	$i_{corr \times 10^{-5}}$ (µA cm^{-2})	$\beta_{a \times 10^{-3}}$ (mV dec^{-1})	$\beta_{c \times 10^{-3}}$ (mV dec^{-1})	θ	% IE
(H₂L)	Blank	505	8.99	79.5	109.3	–	–
	1×10^{-6}	487	2.15	40.6	47.2	0.760	76.0
	3×10^{-6}	483	1.95	102.5	108.4	0.783	78.3
	5×10^{-6}	496	1.61	36.6	49.9	0.820	82.0
	7×10^{-6}	487	1.56	23.3	28.0	0.826	82.6
	9×10^{-6}	482	1.53	18.6	19.9	0.829	82.9
	11×10^{-6}	474	1.23	17.6	21.9	0.863	86.3
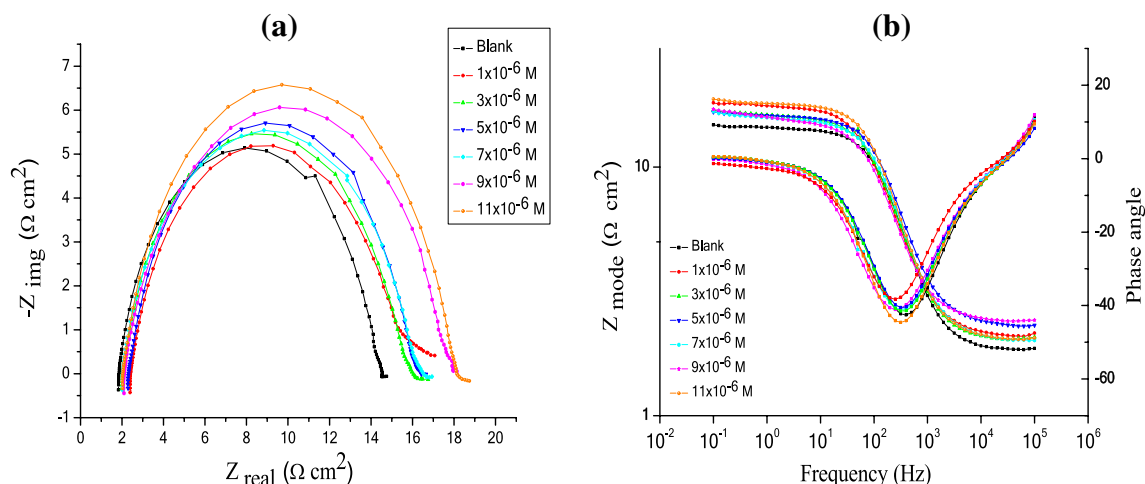
Fig. 14 EIS Nyquist plots (a) and Bode plots (b) for C-steel surface in 2 M HCl attendance and lack of unlike dose of compound (H₂L) at 30 ± 0.1 °C
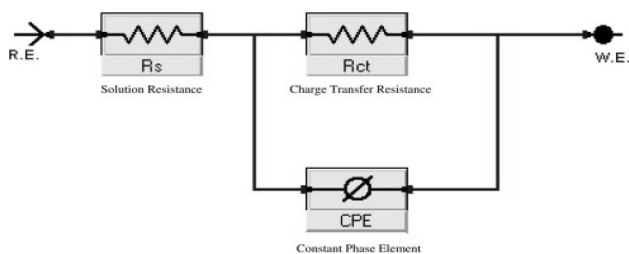
Fig. 15 Equivalent circuit model utilized to fit experimental EIS

Double-layer capacitance data are also brought down to the highest extent in attendance of inhibitor and the lower in the data of CPE obey the same order to that given for i_{corr} in this research. The lower in CPE/C_{dl} outcome from brought down in local dielectric constant and/or improve in the double layer thickness lead to organic derivative preventing the corrosion of C-steel by metal/acid adsorption [94, 95]. The EIS important are to follow the corrosion habit of the metal with time constant. The

Table 17 Electrochemical kinetic parameters given by EIS method for C-steel in 2 M HCl without and with various dose of compound (H₂L) at 30 ± 0.1 °C

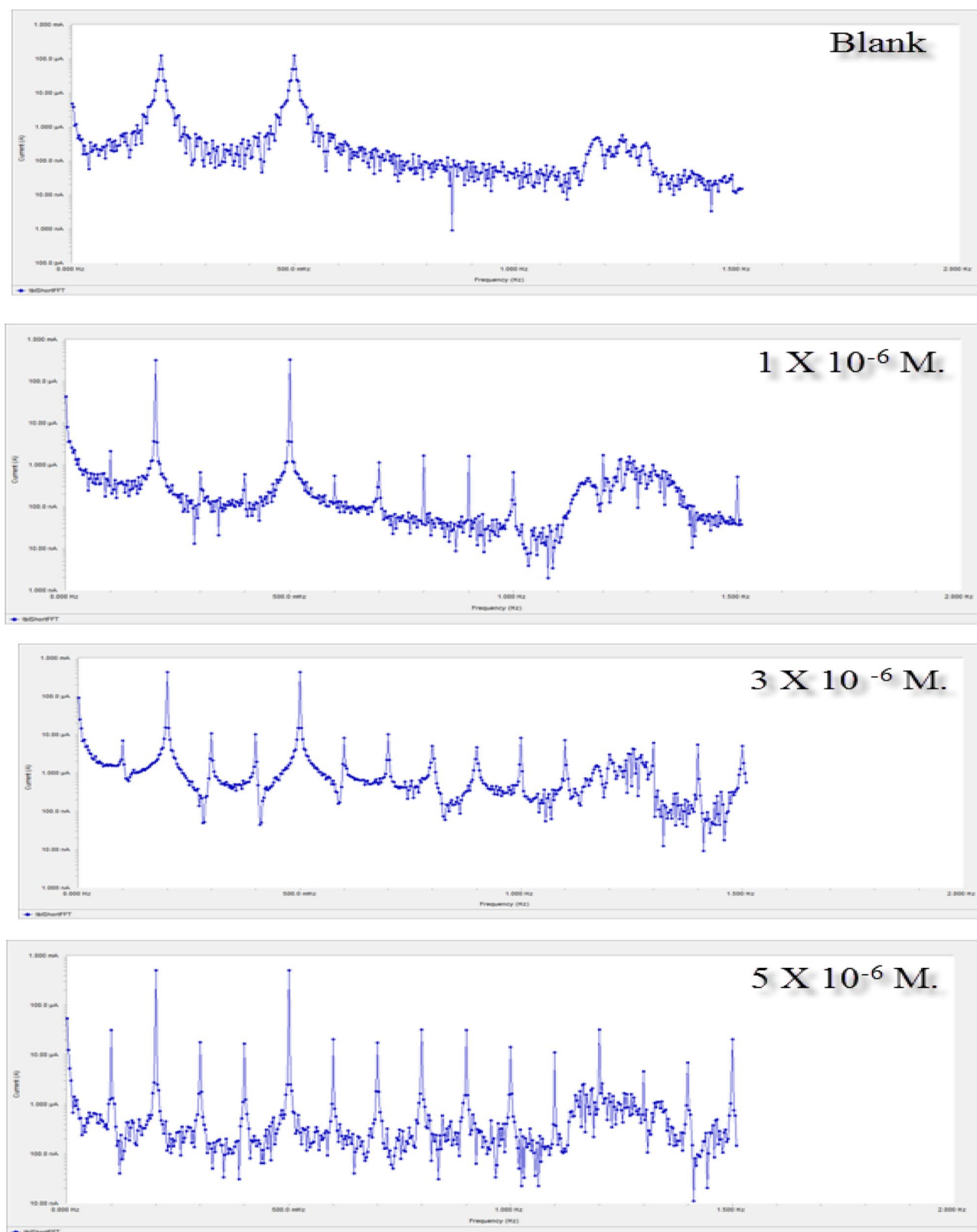| Compound	Conc. (M)	R_S (Ω cm^2)	$Y_{o \times 10^{-4}}$	$n_{\times 10^{-1}}$	R_{ct} (Ω cm^2)	$C_{dl \times 10^{-4}}$ (µFcm^{-2})	θ	%IE
(H₂L)	Blank	1.849	2.38	8.79	12.57	1.07	–	–
	1×10^{-6}	2.162	3.70	8.37	20.44	1.43	0.385	38.5
	3×10^{-6}	2.235	4.64	8.27	21.38	1.77	0.412	41.2
	5×10^{-6}	1.658	1.62	8.80	23.26	0.754	0.460	46.0
	7×10^{-6}	11.09	2.89	8.29	28.71	1.07	0.562	56.2
	9×10^{-6}	12.8	1.03	5.76	39.92	0.989	0.685	68.5
	11×10^{-6}	1.752	2.16	8.48	84.18	1.05	0.851	85.1

Fig. 16 EFM spectra for C-steel in 2 M HCl attendance and lack of unlike dose of compound (H_2L) at 30 ± 0.1 °C
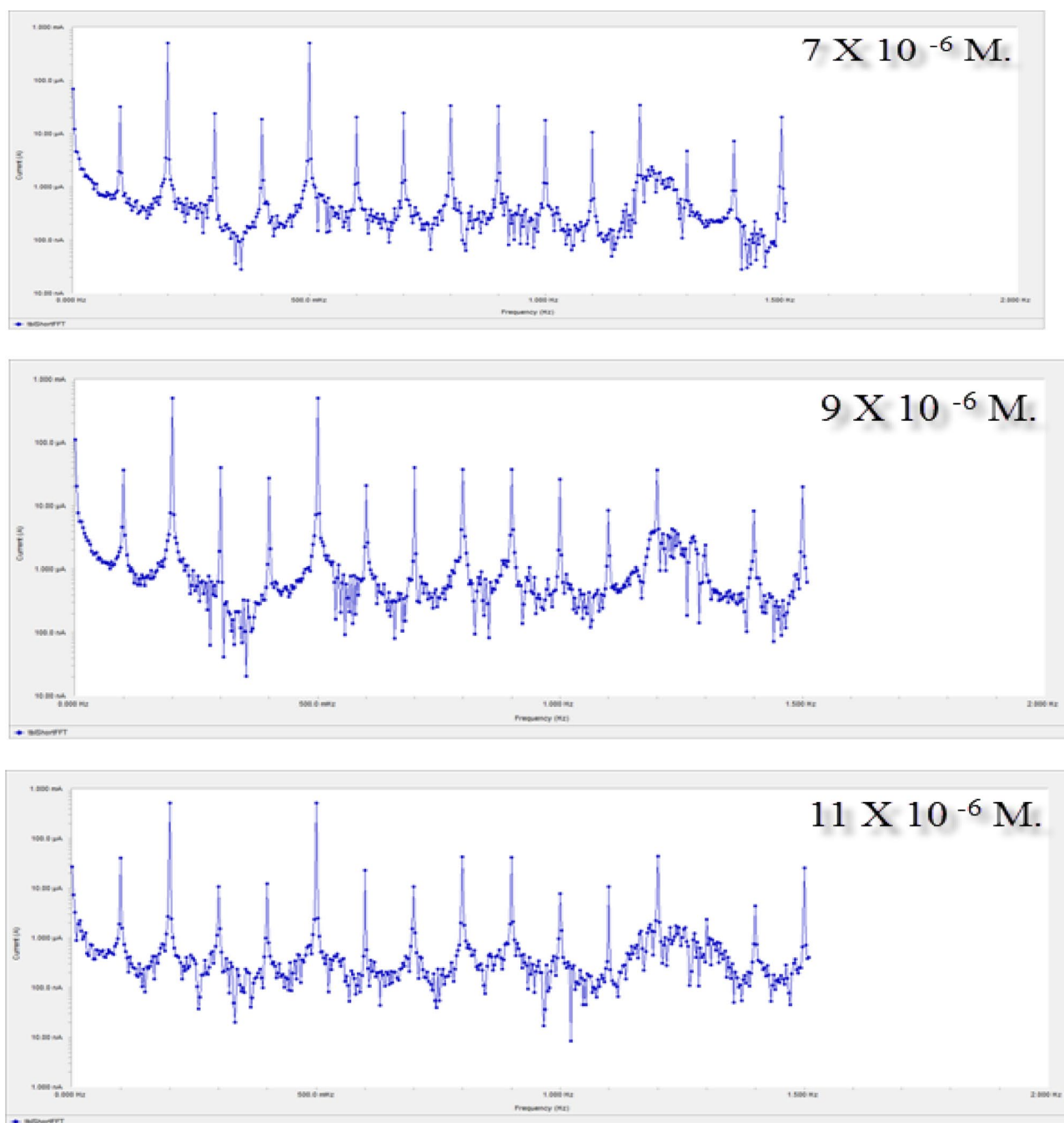
Fig. 16 (continued)

% IE was measured from the charge transfer resistance value from equation [96]:

% $IE_{EIS} = 100 \times [1 - (R^{\circ}_{ct} / R_{ct})]$. where R^{o}_{ct} and R_{ct} are the charge-transfer resistance data attendance and lack of inhibitor, continually.

EFM method

EFM is a nondestructive corrosion analysis method that can undertake and quickly measure the current corrosion data without prior information of Tafel slopes. These important of EFM tests make it real candidate for corrosion online calculation [97]. The causality factors which attend as an internal examine on the exactitude of EFM calculation. The

Table 18 Electrochemical kinetic parameters obtained by EFM tests for C-steel in 2 M HCl without and with unlike dose of compound (H$_2$L) at 30 ± 0.1 °C

Compound	Conc. (M)	i_{corr} (µA cm^{-2})	$\beta_{a \times 10}^{-3}$ (mV dec^{-1})	$\beta_{c \times 10}^{-3}$ (mV dec^{-1})	CF-2	CF-3	θ	%IE
(H$_2$L)	Blank	812.2	40.9	43.1	1.92	2.85	–	–
	1×10^{-6}	269.2	30.3	31.6	1.89	2.64	0.668	66.8
	3×10^{-6}	269.0	28.7	33.9	2.03	3.01	0.669	66.9
	5×10^{-6}	259.9	28.0	30.9	2.02	3.04	0.680	68.0
	7×10^{-6}	253.6	27.0	29.7	2.04	3.33	0.687	68.7
	9×10^{-6}	244.9	25.8	28.1	1.85	2.37	0.698	69.8
	11×10^{-6}	136.3	78.4	29.6	2.09	2.94	0.832	83.2

causality factors CF-2 and CF-3 are measured from the current of frequency spectrum.

Figure 16 gives the EFM spectrums of C-steel in 2 M HCl solution with various dose of inhibitor compound (H$_2$L). The harmonic and intermodulation band are apparent visible and are much higher than the noise of back ground. EFM values were treated utilized two unlike models: perfect control diffusion of the cathodic reaction and the "activation" model. For second, a set of three nonlinear equations had been occurring, assuming that the potential of corrosion does not change because the polarization of the electrode working [98].The larger peaks were utilized to measure the current corrosion density (i_{corr}), (β_c and β_a) and the (CF-3). These electrochemical parameters are record in Table 18.

The value in Table 18 obviously gives that, the appending of any one of tested composite at a given dose to the acidic medium brought down i_{corr} leads to these composite preventing the corrosion of C-steel in 2 M hydrochloric acid by adsorption. The causality factors obtained under unlike tests are nearly equal to the theoretical data (2 and 3) and lead to that the calculated data are perfect and of best quality. % IE$_{EFM}$ improve by rising the inhibitor dose as equation:

$$\%IE_{EFM} = [1 - (i_{corr}/ i^{o}_{corr})] \times 100.$$

where i^{o}_{corr} and i_{corr} are corrosion current densities attendance and lack of inhibitor, respectively.

Conclusions

The complexes of Schiff base ligand (H$_2$L) were characterized by various physicochemical techniques. According to the FT-IR spectra data, it was found that the H$_2$L ligand is coordinated to the metal ions in a tridentate donor sites of the nitrogen atom of azomethine group, the oxygen atom of phenolic group and the oxygen atom of carbonyl group. The XRD patterns of ligand (H$_2$L) and its some complexes showed a lot diffraction peaks which indicate that the polycrystalline phase. Antimicrobial activity of H$_2$L ligand and its complexes were tested against *Staphylococcus aureus* and *Bacillus cereus* as gram-positive bacteria and *Klebsiella pneumoniae, Escherichia coli* and *Pseudomonas* sp.) as gram-negative bacterias well as antifungal activities were determined against *Fusarium oxysporum, Aspergillus niger* and *Candida albicans.* It was found that the complex **(3)** is more active than the antibacterial standard drug (penicillin G) against *Klebsiella pneumoniae*. The complex **(3)** showed very good antibacterial activity in comparison with penicillin G. The results of the molecular docking between the H$_2$L ligand and the receptors of *Staphylococcus aureus* (3q8u) and *Escherichia coli* (3t88) showed a possible arrangement between the receptors (*S. aureus* (3q8u) and *E. coli* (3t88)) and the ligand. The H$_2$L ligand showed similar interaction with *Staphylococcus aureus* (3q8u) receptor than the *E. coli* (3t88) receptor. The inhibition efficiency of the prepared ligand against the corrosion of carbon steel in HCl (2 M) solution was determined by various electrochemical techniques. The experiments corrosion studied the effect of the concentration to ligand and the effect of time on carbon steel in acidic medium, we found by increasing concentration the corrosion decrease but increase by increasing the time. Results obtained from DC polarization, and AC impedance tests are reasonably in best agreement and give rise % IE with the increasing dose of inhibitor. Polarization value showed that the utilized inhibitors play as mixed-kind inhibitor in 2 M HCl.

References

1. A.Z. El-Sonbati, M.A. Diab, A.A. El-Bindary, G.G. Mohamed, Sh.M. Morgan M.I. Abou-Dobara, S.G. Nozha, J. Mol. Liq. **215**, 423 (2016)
2. A.Z. El-Sonbati, M.A. Diab, Sh.M. Morgan, M.I. Abou-Dobara, A.A. El-Ghettany, J. Mol. Str. **1200**, 127065 (2020)

3. A.Z. El-Sonbati, M.A. Diab, Sh.M. Morgan, H.A. Seyam, J. Mol. Str. **1154**, 354 (2018)
4. M.A. Diab, S.G. Nozha, A.Z. El-Sonbati, M.A. El-Mogazy, Sh.M. Morgan, Appl. Organomet. Chem. **33**, e5153 (2019)
5. M.I. Abou-Dobara, N.F. Omar, M.A. Diab, A.Z. El-Sonbati, Sh.M. Morgan, O.L. Salem, A.M. Eldesoky, Mat. Sc. Eng. C **103**, 109727 (2019)
6. T. Rosu, E. Pahontu, C. Maxim, A.P. Gulea, Polyhedron **29**, 757 (2010)
7. S. Bige, Z. Kilie, Z. Hayvali, T. Hokelek, S. Safran, J. Chem. Sci. **121**, 989 (2009)
8. Sh.M. Morgan, A.Z. El-Sonbati, H.R. Eissa, J. Mol. Liq. **240**, 752 (2017)
9. M. Mirzaei, H. Eshtiagh-Hosseini, Z. Karrabi, K. Molčanov, E. Eydizadeh, J.T. Mague, A. Bauzá, A. Frontera, Cryst. Eng. Comm. **16**, 5352 (2014)
10. H. Temel, J. Coord. Chem. **57**, 723 (2004)
11. Sh.M. Morgan, A.Z. El-Sonbati, M.A. El-Mogazy, Appl. Organometal. Chem. **32**, e4264 (2018)
12. N. Tezer, N. Karakus, J. Mol. Model. **15**, 223 (2009)
13. M.A. Diab, A.Z. El-Sonbati, Sh.M. Morgan, M.A. El-Mogazy, Appl. Organometal. Chem. **32**, e4378 (2018)
14. M.I. Abou-Dobara, N.F. Omar, M.A. Diab, A.Z. El-Sonbati, Sh.M. Morgan, M.A. El-Mogazy, J. Cell. Biochem. **120**, 1667 (2019)
15. A.A. Fadda, S. Bondock, R. Rabie, Monatsh. Chem. **13**, 153 (2008)
16. B.H. Amin, M.I. Abou-Dobara, M.A. Diab, E.A. Gomaa, M.A. El-Mogazy, A.Z. El-Sonbati, M.S. EL-Ghareib, M.A. Hussien, H.M. Salama, Appl Organometl Chem **34**, 5689 (2020)
17. S.G. Nozha, Sh.M. Morgan, S.E. Abu Ahmed, M.A. El-Mogazy, M.A. Diab, A.Z. El-Sonbati, M.I. Abou-Dobara, J. Mol. Struct. **1227**, 129525 (2021)
18. A.Z. El-Sonbati, M.A. Diab, Sh.M. Morgan, J. Mol. Liq. **225**, 195 (2017)
19. T.H. Al-Noor, M.R. Aziz, A.T.A.L. Jeboori, Int. J. Techn. Res. Appl. **2**, 187 (2014)
20. G. Thiyagarajan, A. Pandey, P. Mayer, A. Thamaraichelvan, Indi. J. Chem. **53**, 200 (2014)
21. R.O. Shaibu, G.M. Watkins, Ife J. Sci. **17**, 31 (2015)
22. K.J. Donde, J. Chem. Pharm. Res. **7**, 798 (2015)
23. P.A. Vigato, S. Tamburini, Coord. Chem. Rev. **248**, 1717 (2004)
24. N.A. El-Ghamaz, A.Z. El-Sonbati, Sh.M. Morgan, J. Mol. Struct. **1027**, 92 (2012)
25. A.Z. El-Sonbati, M.A. Diab, Sh.M. Morgan, M.Z. Balboula, Appl. Organomet. Chem. **32**, e4059 (2018)
26. N.A. El-Ghamaz, M.A. Diab, A.Z. El-Sonbati, Sh.M. Morgan, O.L. Salem, Chem. Pap. **71**, 2417 (2017)
27. Sh.M. Morgan, N.A. El-Ghamaz, M.A. Diab, J. Mol. Struct. **1160**, 227 (2018)
28. R. Shirley, "The CRYSFIRE system for Automatic Powder Indexing": User's Manual, the Lattice Press, Guildford, Surrey GU2 7NL, England, (2000).
29. H.M. Refaat, H.A. El-Badway, Sh.M. Morgan, J. Mol. Liq. **220**, 802 (2016)
30. G.G. Mohamed, A.A. El-Sherif, M.A. Saad, S.E.A. El-Sawy, Sh.M. Morgan, J. Mol. Liq. **223**, 1311 (2016)
31. M.A. Diab, G.G. Mohamed, W.H. Mahmoud, A.Z. El-Sonbati, Sh.M. Morgan, S.Y. Abbas, Appl. Organometal. Chem. **33**, e4945 (2019)
32. Sh.M. Morgan, M.A. Diab, A.Z. El-Sonbati, Appl. Organometal. Chem. **32**, e4504 (2018)
33. M.I. Abou-Dobara, A.Z. El-Sonbati, Sh.M. Morgan, World J. Microbiol. Biotechnol. **29**, 119 (2013)
34. A.Z. El-Sonbati, N.F. Omar, M.I. Abou-Dobara, M.A. Diab, M.A. El-Mogazy, Sh.M. Morgan, M.A. Hussien, A.A. El-Ghettany, J. Mol. Struct. **1239**, 130481 (2021)
35. A.S. Fouda, A.M. Eldesoky, A.Z. El-Sonbati, S.F. Salam, Int. J. Electrochem. Sci. **9**, 1867 (2014)
36. R.G. Parr, D.A. Donnelly, M. Levy, M. Palke, J. Chem. Phys. **68**, 3801 (1978)
37. R.G. Parr, R.G. Pearson, J. Am. Chem. Soc. **105**, 7512 (1983)
38. A. Pui, C. Pulicar, J.P. Mahy, Inorg. Chim. Acta **360**, 2139 (2007)
39. W.J. Ceary, Coord. Chem Chem. Rev. **7**, 81 (1971)
40. S. Chandan, D. Jain, A.K. Sharma, P. Sharma, Molecules **40**, 174 (2009)
41. R.M. Patil, Acta Pol. Pharm Drug Res. **64**, 345 (2007)
42. A.N. Evstopov, V.E. Yavorovskaya, E.S. Vorobev, Z.P. Kudonogova, L.N. Gritsenko, E.N. Schmidt, S.G. Medvedeva, D.V. Filimonov, T.P. Prishchep, A.S. Saratikov, Pharm. Chem. J. **26**, 426 (1992)
43. Z.H. Abd El-Waheb, M.M. Mashaly, A.A. Faheim, Chem. Pap. **59**, 25 (2005)
44. T. Radmakrishnan, P.T. Joseph, C.P. Prabhakaran, J. Inorg, Nucl. Chem. **38**, 2217 (1976)
45. G. Shankar, R.R. Premkumar, S.K. Ramalingam, Polyhedron **5**, 991 (1986)
46. R. Ramesh, P.K. Suganthy, K. Natarajan, Synth. React. Inorg. Met-Org. Chem. **26**, 47 (1996)
47. A.Z. El-Sonbati, A.A.M. Belal, M.S. El-Gharib, Sh.M. Morgan, Spectrochim. Acta A **95**, 627 (2012)
48. A.Z. El-Sonbati, M.A. Diab, A.A.M. Belal, Sh.M. Morgan, Spectrochim. Acta A **99**, 353 (2012)
49. N.S. Biradar, V.B. Mahale, B.R. Havinale, Curr. Sci. **45**, 124 (1976)
50. A. Syamal, K.S. Kale, Ind. J. Chem. **19A**, 225 (1981)
51. M.A. Ali, A.H. Mirza, M. Nazimuddin, P.K. Dhar, R.J. Butcher, Trans. Met. Chem. **27**, 27 (2002)
52. S.A. Ibrahim, A.M. Hammam, A.M. El-Dean Kamal, A.A. Mohamed, N.M. Rageh, Canadian J. App. Spec. **1**, 38 (1993)
53. A.M. Abdel-Mawgoud, M.M. Hamed, H.M. Mostafa, Monatsh. Chem. **128**, 553 (1997)
54. H.A. Dessouki, M. Gaber, A.L. El-Ansary, Egypt. J. Chem. **32**, 639 (1989)
55. M.R. Mahmoud, S.A. Ibrahim, M.A. Hamed, Spectrochim. Acta A **39**, 729 (1983)
56. E. Hofer, H. Hufimann, Tetrahedron Lett. **35**, 3241 (1971)
57. N. Hassan, A.Z. El-Sonbati, M.G. El-Desouky, J. Mol. Liq. **242**, 293 (2017)
58. A.Z. El-Sonbati, M.A. Diab, A.M. Eldesoky, Sh.M. Morgan, O.L. Salem, Appl. Organometal. Chem. **33**, e4839 (2019)
59. A.Z. El-Sonbati, M.A. Diab, G.G. Mohamed, M.A. Saad, Sh.M. Morgan, S.E.A. El-Sawy, Appl. Organometal. Chem. **33**, e4973 (2019)
60. R.M.N. Badger, J. Chem. Phys. **3**, 710 (1935)
61. L.H. Jones, Spectrochim. Acta A **11**, 409 (1959)
62. A.Z. El-Sonbati, Spetros. Lett. **30**, 456 (1997)
63. S.P. McGlynn, J.K. Smith, W.C. Neely, J. Chem. Phys. **35**, 105 (1961)
64. M. Mirzaei, H. Eshtiagh-Hosseini, A. Bauzá, S. Zarghami, P. Ballester, J.T. Mague, A. Frontera, Cryst. Eng. Comm. **16**(2014), 6149 (2014)
65. F.K. Kneubuhl, J. Chem. Phys. **33**, 1074 (1960)
66. H.R. Garmen, J.D. Swallen, J. Chem. Phys. **56**, 3221 (1962)
67. A. Hassanpoor, M. Mirzaei, M.N. Shahrak, A.M. Majcher, Dalton Trans. **47**, 13849 (2018)
68. A. Hassanpoor, Masoud Mirzaei, Hossein Eshtiagh-Hosseini, Anna Majcher. Cryst. Eng. Comm. **20**, 3711 (2018)
69. A.B.P. Lever, *Inorganic Electronic Spectroscopy* (Elsevier, Amsterdam, 1968)

70. H. Eshtiagh-Hosseini, M. Mirzaei, S. Zarghami, A. Bauzá, A. Frontera, J.T. Mague, M. Habibi, M. Shamsipur, Cryst. Eng. Comm. **16**, 1359 (2014)
71. A.H. Maki, B.R. McGarvey, J. Chem. Phys. **29**, 31 (1958)
72. A.B.P. Lever, Mantovani. Inorg. Chem. **10**, 817 (1971)
73. A.Z. El-Sonbati, M.A. Diab, Sh.M. Morgan, M.A. El-Mogazy, Appl Organometal Chem **32**, e4530 (2018)
74. A.Z. El-Sonbati, M.A. Diab, Sh.M. Morgan, A.M. Eldesoky, M.Z. Balboula, Appl Organometal. Chem **32**, e4207 (2018)
75. A.Z. El-Sonbati, W.H. Mahmoud, G.G. Mohamed, M.A. Diab, Sh.M. Morgan, S.Y. Abbas, Appl. Organometal. Chem. **33**, e5048 (2019)
76. Sh.M. Morgan, M.A. Diab, A.Z. El-Sonbati, Appl. Organometal. Chem. **32**, e4305 (2018)
77. Sh.M. Morgan, M.A. Diab, A.Z. El-Sonbati, Appl. Organometal. Chem. **32**, e4281 (2018)
78. J. Laugier and B. Bochu, LMGP-suite suite of programs for the interpretation of X-ray experiments, ENSP/Laboratoire des Materiauxet du genie physique, Saint Martin d'Heres, France, 2000, pp. BP46.38042.
79. H. Eshtiagh-Hosseini, M. Mirzaei, M. Biabani, V. Lippolis, M. Chahkandi, C. Bazzicalupi, Cryst. Eng. Comm. **15**, 6752 (2013)
80. A.W. Coats, J.P. Redfern, Nature **201**, 68 (1964)
81. H.H. Horowitz, G. Metzger, Anal. Chem. **35**, 1464 (1963)
82. M.A. Diab, A.Z. El-Sonbati, N.A. El-Ghamaz, Sh.M. Morgan, O. El-Shahat, Eur. Polym. J. **115**, 268 (2019)
83. A.B.P. Lever, E. Mantovani, Inorg. Chem. **10**, 817 (1971)
84. M.A. Al-Khaldi, K.Y. Al-qahtani, J. Mater. Environ. Sci. **4**(5), 593 (2013)
85. A.S. Fouda, M.A. Diab, A.Z. El-Sonbati, S.A. Hassan, J. Electrochem. Sci. **12**, 5072 (2017)
86. D.D. Macdonald, M.C.H. Mckubre, "Impedance measurements in electrochemical systems" Modern Aspects of Electrochemistry, J.O'M. Bockris, B.E. Conway, R.E. White, Eds., Plenum Press, New York 14 1982 pp. 61–150.
87. F. Mansfeld, Corrosion **36**, 301 (1981)
88. C. Gabrielli, "Identification of Electrochemical processes by Frequency Response Analysis" Solarton Instrumentation Group, 1980.
89. M. El Achouri, S. Kertit, H.M. Gouttaya, B. Nciri, Y. Bensouda, L. Perez, M.R. Infante, K. Elkacemi, Prog. Org. Coat. **43**, 267 (2001)
90. A. Anejjar, A. Zarrouk, R. Salghi, H. Zarrok, D. Ben Hmamou, B. Hammouti, B. Elmahi, S.S. Al-Deyab, the ecidenc. J Mater Environ Sci **4**, 583 (2013)
91. S.F. Mertens, C. Xhoffer, B.C. Decooman, E. Temmerman, Corrosion **53**, 381 (1997)
92. G. Trabanelli, C. Montecelli, V. Grassi, A. Frignani, J. Cem. Concr. Res. **35**, 1804 (2005)
93. F.m. Reis, H.G. de Melo, I. Costa, J. Electrochem. Acta 51 (2006) 1780.
94. E. McCafferty, N. Hackerman, J. Electrochem. Soc. **119**, 999 (1972)
95. A.S. Fouda, M.A. Diab, A.Z. El-Sonbati, Sh.A. Hassan, Int. J. Electrochem. Sci. **12**, 5072 (2017)
96. H. Ma, S. Chen, L. Niu, S. Zhao, S. Li, D. Li, J. Appl. Electrochem. **32**, 65 (2002)
97. E. Kuş, F. Mansfeld, Corros. Sci. **48**, 965 (2006)
98. G.A. Caigman, S.K. Metcalf, E.M. Holt, J. Chem. Cryst. **30**, 415 (2000)